CO Abundance Variations in the Orion Molecular Cloud

F. Ripple[1], M. H. Heyer[1], R. Gutermuth[1], R.L. Snell[1], C.M. Brunt[2]

[1] *Department of Astronomy, University of Massachusetts, Amherst, MA 01003, USA*
[2] *School of Physics, University of Exeter, Exeter, EX4 4QL, UK*

13 February 2013

ABSTRACT
Infrared stellar photometry from the Two Micron All Sky Survey (2MASS) and spectral line imaging observations of ^{12}CO and ^{13}CO J = 1-0 line emission from the Five College Radio Astronomy Observatory (FCRAO) 14m telescope are analysed to assess the variation of the CO abundance with physical conditions throughout the Orion A and Orion B molecular clouds. Three distinct A_v regimes are identified in which the ratio between the ^{13}CO column density and visual extinction changes corresponding to the photon dominated envelope, the strongly self-shielded interior, and the cold, dense volumes of the clouds. Within the strongly self-shielded interior of the Orion A cloud, the ^{13}CO abundance varies by 100% with a peak value located near regions of enhanced star formation activity. The effect of CO depletion onto the ice mantles of dust grains is limited to regions with $A_v > 10$ mag and gas temperatures less than $\sim$20 K as predicted by chemical models that consider thermal-evaporation to desorb molecules from grain surfaces.

Values of the molecular mass of each cloud are independently derived from the distributions of A_v and ^{13}CO column densities with a constant ^{13}CO-to-H$_2$ abundance over various extinction ranges. Within the strongly self-shielded interior of the cloud ($A_v > 3$ mag), ^{13}CO provides a reliable tracer of H$_2$ mass with the exception of the cold, dense volumes where depletion is important. However, owing to its reduced abundance, ^{13}CO does not trace the H$_2$ mass that resides in the extended cloud envelope, which comprises 40-50% of the molecular mass of each cloud. The implied CO luminosity to mass ratios, M/L_{CO}, are 3.2 and 2.9 for Orion A and Orion B respectively, which are comparable to the value (2.9), derived from γ-ray observations of the Orion region. Our results emphasize the need to consider local conditions when applying CO observations to derive H$_2$ column densities.

Key words: ISM: abundances – ISM: clouds – ISM: individual – ISM: molecules – radio lines: ISM

1 INTRODUCTION

The mass and column density of interstellar molecular clouds impact their evolution, chemistry, and the production of newborn stars within their domain. Therefore, accurate measures of these key properties are essential to our understanding of this important interstellar gas phase. The millimeter and submillimeter rotational transitions of carbon monoxide (^{12}CO) and its isotopologues, ^{13}CO and C^{18}O, are the most widely used tracers of molecular hydrogen (H$_2$) that offer several advantages over other methods such as dust extinction, dust emission, and gamma rays. These include the ability to construct high angular resolution views of distant interstellar molecular clouds throughout the Milky Way and other galaxies, and with sufficient spectral resolution, the provision of critical kinematic information such as the velocity centroid and velocity dispersion for a given line of sight. Measurements of the optically thick ^{12}CO J=1-0 line are routinely made in investigations of star formation processes in galaxies (Young et al. 1995; Omont 2007; Leroy et al. 2009). The application of this high opacity line as a tracer of molecular hydrogen relies on the empirical correlation between ^{12}CO velocity integrated intensity, W$_{CO}$, and γ-ray intensity that is produced from the interaction of cosmic rays with hydrogen protons within the Milky Way (Bloemen et al. 1986; Strong & Mattox 1996; Hunter et al. 1997). The corresponding CO to H$_2$ conversion factor, X_{CO}=N(H$_2$)/W$_{CO}$ is 1.9×10^{20} cm^{-2} (K km s^{-1})$^{-1}$ (Strong & Mattox 1996). A similar procedure has been followed using the dust emission to trace gas column density with derived values of X_{CO} ranging from 1.8-2.5$\times 10^{20}$ cm^{-2} (K km s^{-1})$^{-1}$ (Dame, Hartmann, & Thaddeus 2001; Ade et al. 2011).

Emission from ^{13}CO offers another measure of the

molecular gas distribution. Owing to its lower opacity, it is straightforward to derive the ^{13}CO column density under the assumption of local thermodynamic equilibrium (LTE), using the optically thick ^{12}CO line to estimate the excitation temperature (Dickman 1978). However, to derive the more relevant H_2 column density and mass, knowledge of the ^{13}CO abundance is required. Most studies adopt a constant fractional abundance of $\sim 2 \times 10^{-6}$ throughout the cloud based on previous investigations of nearby dark clouds, which examined the relationship between ^{13}CO column density and visual extinction (Dickman 1978; Frerking, Langer, & Wilson 1982). These earlier studies investigated the N(^{13}CO)-A_v relationship in cold, dark clouds with limited star formation activity.

In this paper, we examine the relationship between carbon monoxide and near infrared extinction in the Orion molecular cloud that is producing massive stars and presents a broad range of environmental conditions. In Section 2, we describe the near-infrared and molecular line data used in this study. The procedures used to derive extinctions from the 2MASS colours and the ^{13}CO column densities from the molecular line imaging are summarized in Section 3. In Section 4 the results of point-to-point comparison of the ^{13}CO column density and ^{12}CO integrated intensity to visual extinction relation are presented. The interpretation of these relationships within the context of photon-dominated regions (PDRs) models, the calculation of relative abundances, and the derivation of cloud masses are described in Section 5.

2   DATA

2.1   Millimeter Spectroscopic Imaging

Observations of ^{12}CO and ^{13}CO J=1-0 emission were carried out with the FCRAO 14m telescope using the 32 pixel SEQUOIA array (Erickson et al. 1999) between 2005 and 2006. Owing to the broad bandwidth of the HEMT amplifiers, the ^{12}CO and ^{13}CO lines were observed simultaneously enabling excellent positional registration and calibration. The backends were comprised of 64 autocorrelation spectrometers each with 25 MHz bandwidth. No smoothing was applied to the autocorrelation function so the spectral resolution was 29.5 kHz per channel corresponding to 0.077 km s^{-1} and 0.080 km s^{-1} at the line frequencies of ^{12}CO (115.271202 GHz) and ^{13}CO (110.201353 GHz) respectively. System temperatures ranged from 350-500 K (^{12}CO) and 150-300 K (^{13}CO). The FWHM beam size of the antenna at the observed frequencies are $45''$ (115 GHz) and $47''$ (110 GHz). The main beam efficiencies at these frequencies are 0.45 and 0.48 respectively as determined from measurements of Jupiter.

The areas of the Orion A and Orion B clouds were divided into submaps. A given submap of ^{12}CO and ^{13}CO emission was constructed by scanning the telescope at an angle $\theta_s = 14.04$ degrees relative to the azimuth direction. This choice of scanning angle ensures even coverage of the sky along a single scan. Subsequent scans are orthogonally offset by the entire width of the array to extend the sky coverage. We also employed scanning angles of $\theta_s + 90$. A basic observational block was comprised of a sequence of scans

either using θ_s or $\theta_s + 90$. Submaps were observed so that adjacent blocks overlap. The scanning angle for each block was set to be opposite to that of its neighboring block. The angular coverage spanned 22.2 deg^2 for Orion A and 17.4 deg^2 for Orion B. The 1σ errors due to thermal noise (main beam temperature units) within 0.2 km s^{-1} wide channels are 2.0 K (Orion A) and 2.1 K (Orion B) for ^{12}CO and 0.77 K (Orion A) and 0.85 K (Orion B) for the ^{13}CO data.

Images of velocity integrated ^{12}CO and ^{13}CO J=1-0 emission from the Orion A and Orion B clouds at the full angular resolution are shown in Figure 1 and Figure 2 respectively. The irregularly shaped boundaries result from the scanning method. Data near the boundaries exhibit higher noise owing to less integration time. The images show several common emission features typical of giant molecular clouds. Regions of bright, high contrast emission are typically sites of the most recent star formation. Such regions are often warm ($T_k > 25$ K), filamentary, and characterized by high column densities (N(H_2) $> 10^{22}$ cm^{-2}). In addition, there is an extended, low surface brightness component that comprises most of the projected area of the cloud. Recent wide field imagery of ^{12}CO and ^{13}CO J=3-2 emission from Orion A shows similar, large scale features (Buckle, et al. 2009, 2012). Our wide field data on Orion B offers a significant improvement in sensitivity, angular and spectral resolution over previous maps of CO emission (Bally, Langer, & Liu 1991)

2.2   Near-infrared Photometry

Near-infrared extinctions are determined from colours of stars listed in the Point Source Catalog of the Two Micron All-Sky Survey (2MASS) (Skrutskie et al. 2006). The observations are comprised of three near-infrared bands: J (1.24μm), H (1.66μm), and K_s (2.16μm). The 2MASS Point Source Catalog achieves 99% differential completeness limits of 15.8, 15.1, and 14.3 magnitudes for J, H, and K_S bands respectively with 5% photometric accuracy for bright sources and $0''.5$ positional accuracy relative to the International Celestial Reference System (ICRS). Positions and photometric information are extracted from the 2MASS Point Source Catalog for objects that coincide with the area covered by the molecular line observations shown in Figure 1 and Figure 2. The Orion A and Orion B fields contain 164,930 and 242,931 sources respectively. In addition, six circularly shaped control fields with radius of $1°$ are analysed. These fields are selected based on their large angular displacement from known regions of molecular emission. The (l, b) centre positions of each control field are: (204, -22), (220,-20), (212,-23), (214,-16), (215,-23), and (220,-16). Only stars with detections in all three bands and with photometric errors less than 0.03 magnitudes are used for the control field, resulting in a total of 26,927 stars.

3   ANALYSIS

3.1   Gas Excitation and ^{13}CO Column Density

Methods to derive column densities of ^{13}CO from observations of the low rotational quantum numbers under the assumption of Local Thermodynamic Equilibrium
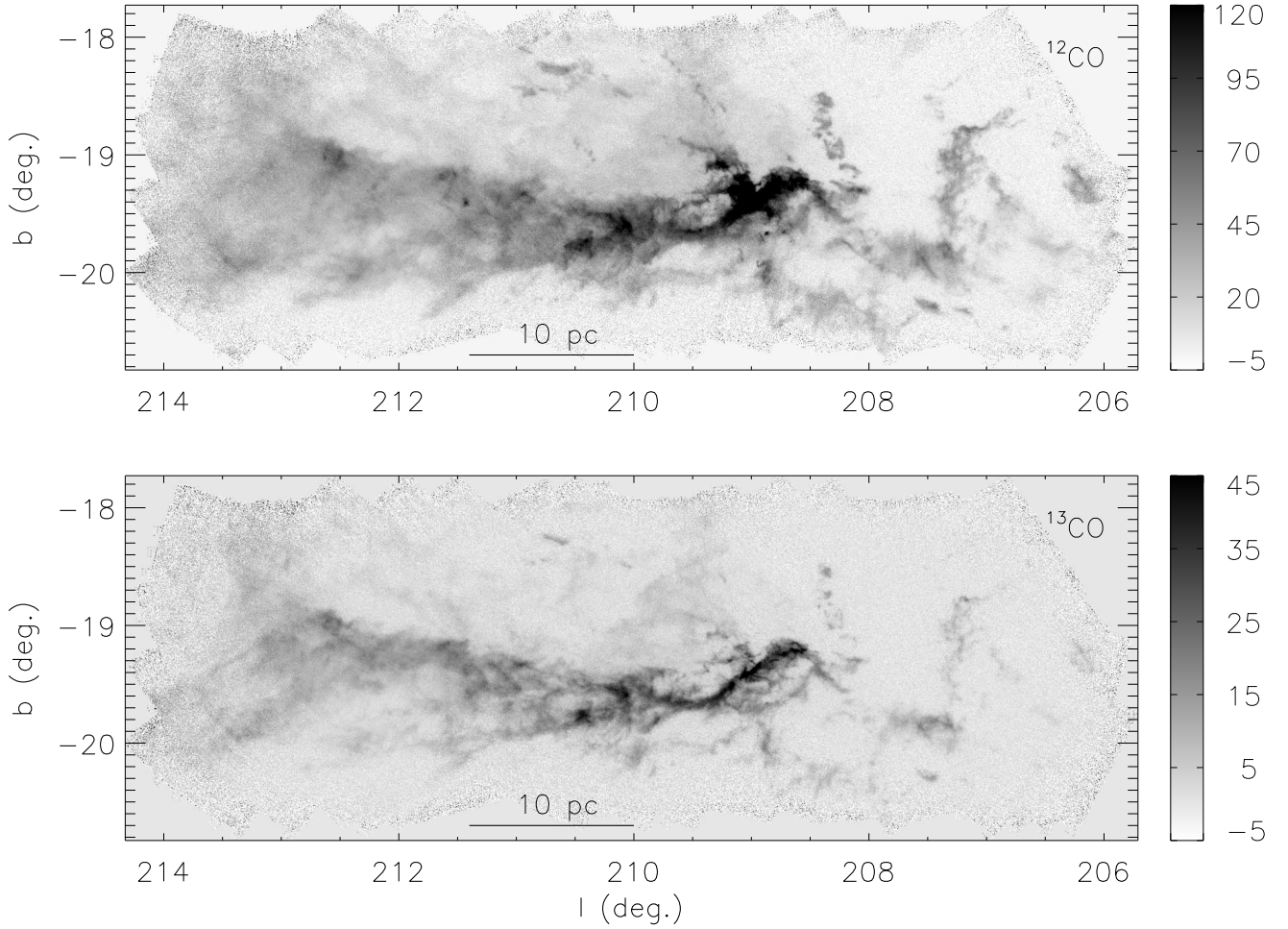
Figure 1. Images of (top) ^{12}CO and (bottom) ^{13}CO J=1-0 emission from the Orion A molecular cloud integrated over V_{LSR} 0 to 16 km/s at the full resolution of the observations. Units of the colour wedges are $Kkms^{-1}$.

(LTE) are provided by Dickman (1978) and more recently, Pineda et al. (2010)[1]. In brief, the excitation temperature that characterizes the population levels of the lower and upper rotational states of ^{13}CO is determined from the peak brightness temperature of the optically thick ^{12}CO line, $T_{12,pk}$. For the J=1-0 transition,

$$T_{ex} = \frac{5.53}{ln(1 + \frac{5.53}{T_{12,pk}+0.83})} \qquad (1)$$

The opacity of the ^{13}CO emission, $\tau_{13,1}(v)$, in the upper, J=1 rotational state is derived from the ^{13}CO brightness temperature, $T_{13}(v)$,

$$\tau_{13,1}(v) = -ln\left[1 - \frac{T_{13}(v)}{5.29}([e^{5.29/T_{ex}} - 1]^{-1} - 0.16)^{-1}\right] \quad (2)$$

The column density of ^{13}CO within the J=1 state, N_1, is given by the expression

$$N_1 = \frac{8\pi k\nu^2}{hc^3 A_{10}} \left[\frac{\int \tau_{13,1}(v)dv}{\int(1 - exp(-\tau_{13,1}(v)))dv}\right] \int T_{13}(v)dv \qquad (3)$$

where A_{10} is the Einstein A coefficient and ν is the frequency of the J=1-0 transition. To account for column density in the other rotational states, the assumption of LTE is applied,

$$N(^{13}CO) = N_1 \frac{Z}{2J+1} e^{-hB_\circ \frac{J(J+1)}{kT_{ex}}} \qquad (4)$$

where $B_\circ$ is the rotational constant for ^{13}CO, and Z is the partition function,

$$Z = \sum_{J=0}^{\infty} (2J+1)e^{-hB_0 \frac{J(J+1)}{kT_{ex}}} \qquad (5)$$

The uncertainties in the ^{13}CO column densities are dominated by the assumptions of LTE. For regions with densities less than the critical density, the ^{13}CO rotational
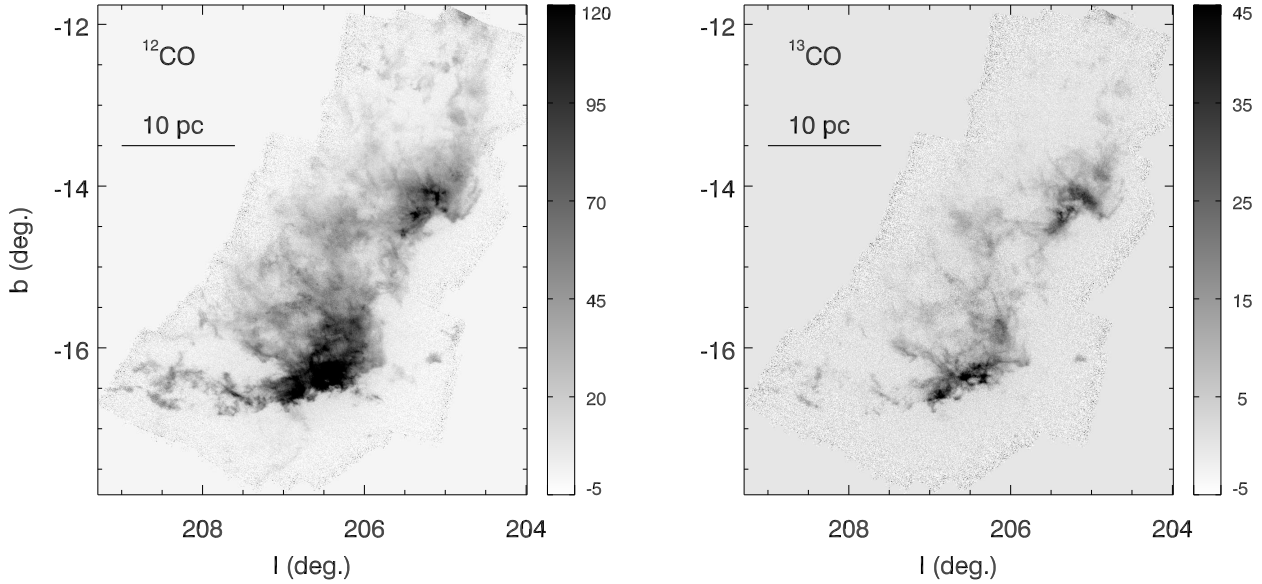
[1] There is a typo in equation 18 of Pineda et al. (2010). The argument to the exponential function should read $J(J+1)/kT_x$.

Figure 2. Images of (left) ^{12}CO and (right) ^{13}CO J=1-0 emission from the Orion B molecular cloud integrated over V_{LSR} 0 to 16 km/s at the full resolution of the observations. Units of the colour wedges are $Kkms^{-1}$.

energy levels may be subthermally excited. Thus, the excitation temperature derived from the more thermalized ^{12}CO J=1-0 line may overestimate the excitation temperature of ^{13}CO. To illustrate this effect, we solve for the population in the ^{13}CO rotational energy levels using an escape probability radiative transfer method with the following conditions: volume density of 750 cm^{-3}, H$_2$ column density of 3×10^{21} cm^{-2}, a kinetic temperature of 10 K, a ^{13}CO to H$_2$ abundance of 2×10^{-6}, and a velocity dispersion of 0.4 km s^{-1}. The model excitation temperatures for the J=1-0 transition are 9.8 K for ^{12}CO and 5.5 K for ^{13}CO. In this case of subthermal excitation, the optical depth correction for ^{13}CO is underestimated leading to a smaller column density in the J=1 level. This error is partially compensated by the overcorrection for population of the higher excited states using a higher excitation temperature. For a spectrum with a peak antenna temperature of 1.5 K, the ^{13}CO LTE column density derived using the ^{12}CO excitation temperature of 9.8 K is 0.7 times the column density using T_{ex}=5 K.

To assess the impact of the thermal noise inherent within the observations, we derive the excitation temperature and ^{13}CO column density using a Monte Carlo method that estimates the statistical errors for each quantity. The calculations are performed on data cubes of the ^{12}CO and ^{13}CO J=1-0 emission that are re-sampled to 1.8′ pixel size and angular resolution. This resolution element corresponds to the pixel size of the infrared extinction map described in §3.2. For each location on the sky, values of peak ^{12}CO brightness temperatures and ^{13}CO integrated intensities are extracted from Gaussian distributions centered on the measured value of the peak temperature of the ^{12}CO spectrum, $T_{12,pk}$, and $W(^{13}CO) = \int T_{13}(v)dv$ with dispersions of σ_{12} and $\sigma_{13}\sqrt{\Delta v \delta v}$ where σ_{12} and σ_{13} are the root mean-square values of antenna temperatures in spectral channels with

no emission, Δv is the channel spacing for each spectrum and δv is the velocity width over which the ^{13}CO spectrum is integrated. In this study, we consider the V_{LSR} interval of 0 to 16 km s^{-1} so δv=16 km s^{-1}. A given set of $T_{12,pk}$ and $W(^{13}CO)$ values are propagated through equations 1-5 to produce realizations of T_{ex} and N(^{13}CO). This step is repeated 1024 times to generate distributions of T_{ex} and N(^{13}CO) values for each pixel. The value of the excitation temperature and statistical error at a given position, x,y, is respectively, the mean and dispersion of the T_{ex} distribution. Similarly, the mean and dispersion of the N(^{13}CO) distribution are assigned to the ^{13}CO column density and its statistical error respectively. Images of the excitation temperature and ^{13}CO column density are shown in Figure 3 for Orion A and Figure 4 for Orion B. Median 1-sigma uncertainties for T_{ex} and N(^{13}CO) in Orion A are 0.59 K and 5×10^{14} cm^{-2} respectively. For Orion B, these values are 0.55 K and 6×10^{14} cm^{-2}.

3.2   Visual Extinction

The 2MASS Point Source Catalog is a powerful set of data to construct extinction images of nearby interstellar clouds. As an all sky survey, it covers the wide area subtended by nearby clouds. In addition, a greater number of background sources are detected in the near infrared relative to optical bands owing to the reduced opacity with increasing wavelength. To derive extinctions to each star, we implement the Near-Infrared Color Excess Revisited (NICER) method described by Lombardi & Alves (2001). This method is a multi-band, maximum-likelihood approach for determining extinction to a background star based on the near-infrared colours. This is achieved through comparison of the observed stellar colour, c_i^{obs}, with the intrinsic colour, c_i^{int} derived
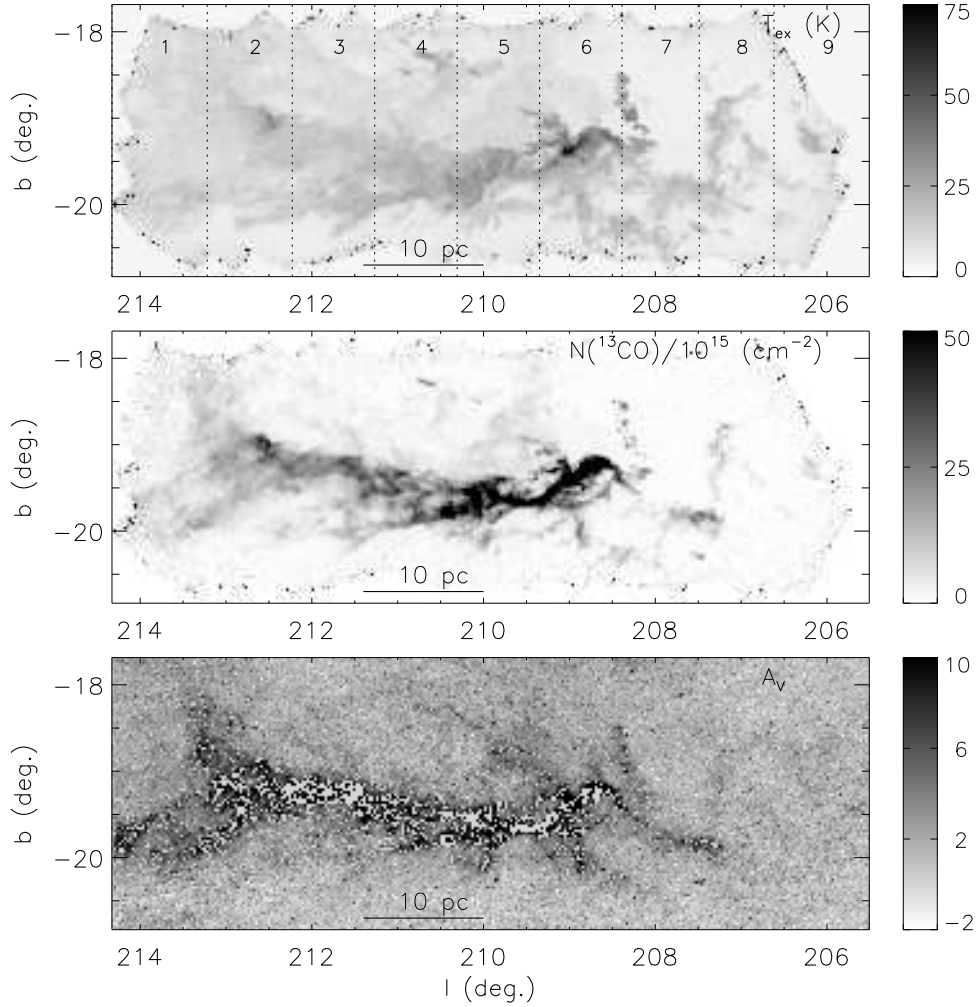
Figure 3. Images of (top) gas excitation temperature, (middle) ^{13}CO column density, and (bottom) infrared derived visual extinction after applying the clipping algorithm for Orion A. Pixels for which the extinction is not defined are blanked and shown as white coloured pixels. These are located in the high column density regions of the cloud. The vertical dotted lines and numbers in the T_{ex} image denote the partitions discussed in the text.

from stars within a control field assumed to have no reddening. With the three near infrared bands of 2MASS, two colours: $c_1 = J - H$ and $c_2 = H - K_S$, are calculated. The inferred V-band extinction is derived from the measured colour excess as

$$A_{v,i} = \frac{(c_i^{obs} - c_i^{int})}{k_i} \qquad (6)$$

where k_i represents the ratio between the colour excess and the V band extinction. We adopt the reddening law from Rieke & Lebofsky (1985), corresponding to $k_1 = 1/9.35$ and $k_2 = 1/15.87$. The NICER method has the advantage of using any number of colours depending on the data available. Extinctions are derived in cases where photometric data are only available in two of the three bands.

The intrinsic stellar J-H and H-K_S colours and colour variance of background stars are derived from stellar photometry within the control fields. The mean colours and

standard deviations for stars within the control fields are: 0.446 ± 0.158 mag and 0.112 ± 0.058 mag for (J-H) and (H-K_S).

For each star in the target field, the NICER procedure produces an extinction, A_v, and its variance, $Var(A_v)$, that considers both the variance of colours in the control fields and the photometric errors of the target star. The uncertainty of these extinction estimates, $\sigma_{A_v} = \sqrt{Var(A_v)}$, is dominated by the variance of the intrinsic colours of control field stars rather than the photometric errors of the target star. The median of derived extinction uncertainty values is 1.4 magnitudes for both the Orion A and Orion B clouds.

There are several sources of contamination to identify and remove prior to folding the derived extinction values into an image to compare with the ^{13}CO column density image. As the Orion cloud is an active region of star formation, one expects a number of young stellar objects (YSOs) at various stages of pre-main sequence evolution within the
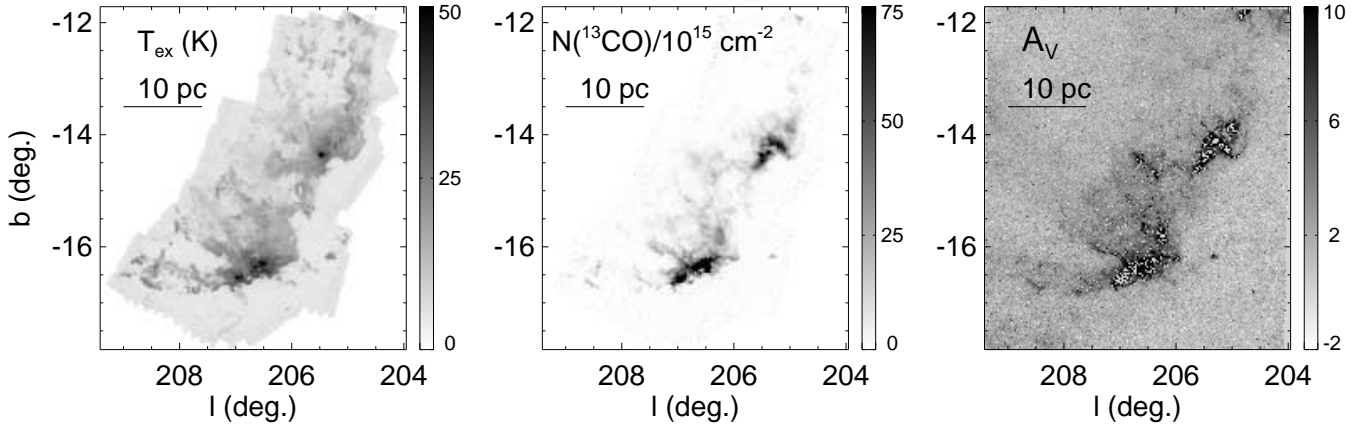
Figure 4. Images of (left) gas excitation temperature, (middle) ^{13}CO column density, and (right) visual extinction for Orion B.

observed fields. Class I and II YSOs are associated with large infrared excesses due to the presence of a dense envelope or circumstellar disk that both attenuates the photospheric emission of the star and contributes to the near infrared flux from warm, thermally emitting dust grains. Therefore, the extinction inferred from the infrared excess of Class I and Class II YSOs is not representative of the column density through the ambient cloud. In Orion A, the degree of contamination by YSOs is particularly acute near the Orion Nebula Cluster. The catalog of Class I and II YSOs generated by Megeath et al. (2012) derived from longer wavelength photometry from the Spitzer Space Telescope, is used to remove such objects from the list of background stars. A total of 2,456 (Orion A) and 553 (Orion B) Class I and Class II YSOs are excluded from our analysis.

More problematic sources of contamination are foreground stars and Class III YSOs within the cloud. Both stellar types have intrinsic colours comparable to those derived in the control fields but whose light is not extincted by the full path of the cloud, if at all. The effect of including such stars in deriving the local extinction is illustrated in Figure 5, which shows a rare but extreme example of such contamination. A_v values derived for stellar sources contained within a $1.8' \times 1.8'$ area of the cloud are rank-ordered for clarity. The low extinctions determined for 5 stars is discrepant by ~ 20 magnitudes with the large A_v values of four stars as well as the equivalent extinction based on the ^{13}CO column density, $A_{v,eq}$=N(^{13}CO)/2.0 x 10^{15} mag^{-1} (Dickman 1978). While such extinction differences could be due to intrinsic, cloud structure within the area of the pixel, we attribute these discrepancies to contamination by foreground stars and Class III pre main sequence stars that are surely present within the Orion cloud that has been actively forming stars for several million years. Using extinction maps of star forming clouds at varying distances, Lombardi, Alves, & Lada (2011) estimate 279 foreground stars per square degree towards the Orion cloud. This corresponds to 0.25 foreground stars per $1.8'$ sized pixel. Owing to magnetic activity in their atmospheres, Class III YSOs can be identified by their X ray emission. A list of X-ray identified Class III stars in Orion A (L1641 and NGC 1980)

has been compiled from XMM-Newton data (Pillitteri et al. 2012). In total, 443 Class III stars from this list have 2MASS counterparts and are excluded from our data analysis.

The X ray survey of the Orion A cloud does not provide a complete census of Class III YSOs nor does it identify foreground stars. To isolate and remove additional Class III YSOs and foreground stars, we apply the following algorithm that conservatively leverages the additional information provided by the ^{13}CO column density. If $A_{v,eq}$ is greater than an extinction threshold, $A_{v,th}$, and the extinction of any star within the $1.8'$ pixel is less than a fraction of the equivalent extinction, $f_{th}A_{v,eq}$, then the star is excluded from any subsequent analysis. Optimal values for $A_{v,th}$ and f_{th} are determined by maximizing the number of X-ray emitting Class III YSOs identified by the algorithm. From this optimization, we find $A_{v,th} = 8$ mag and $f_{th} = 30\%$, which identifies 56% of the 443 known Class III stars. The algorithm is illustrated in Figure 5. The solid line shows the $A_{v,eq}$ estimated from N(^{13}CO) and the dotted line shows $A_{v,th}$ below which our algorithm would remove stars. Following the removal of the contaminating stars, the mean extinction shifts from 8.7 (dashed line) to 18.2 magnitude (dotted-dashed line). A more liberal cut by increasing $A_{v,th}$ and/or f_{th} would increase the likelihood of removal of valid background stars. The algorithm is limited to regions with large ^{13}CO column densities. Applying the algorithm to all stars, 2090 additional, potentially contaminating stars (1.1% of total) are isolated and removed from the list of background stars for Orion A. For Orion B, 824 contaminated sources are culled from this list. Contamination by foreground and/or embedded sources may still be present in regions of lower ^{13}CO column density.

An image of dust extinction is created from the set of infrared colours of background stars within our final list following the removal of YSOs and foreground stars. Spatial grids are setup that are aligned with the respective images of ^{13}CO column density with $1.8'$ size pixels. The extinction of all sources whose position falls within the solid angle subtended by the pixel are averaged with equal weighting. The resultant image has a fixed resolution throughout the map at the expense of variable noise owing to a varying number
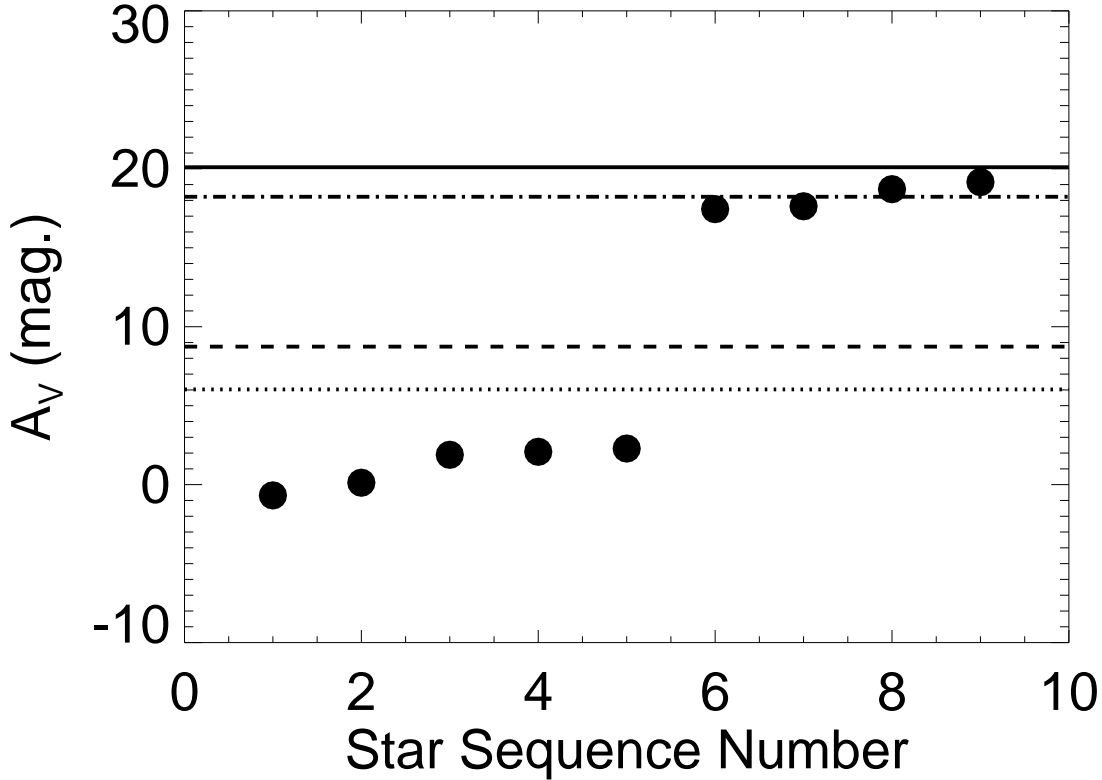
Figure 5. The rank-ordered values of derived extinction for 9 stars contained within a 1.8×1.8′ area. The effect of contaminating foreground and diskless YSO sources is to lower the mean extinction. The heavy solid line represent the A_v value determined from ^{13}CO, the dotted line shows the threshold, $A_{v,th}$ of the clipping algorithm, the dashed lined denotes the mean extinction value before the cut, and the dotted-dashed line shows the mean extinction value after removing the contaminating sources.

of extinction values that are averaged. The median 1σ extinction errors for these sized pixels for $A_v < 10$ are 0.8 mag and 0.7 mag for Orion A and Orion B respectively. For $A_v \geqslant 10$, the median extinction error is 1 mag for both clouds. These values are the propagation of the random errors for the set of extinctions that are averaged into a pixel. The standard deviation of the set of extinction values is typically larger than the associated random error. For extinctions less than 10 mag., the median dispersions are 1.2 and 1.4 magnitudes for Orion A and Orion B respectively. For $A_v > 10$, the dispersions are 2.5 and 2.3 magnitudes. In high extinction regions, there are many pixels through which no background stars shine. In these cases, the pixel is blanked and excluded from all subsequent analyses. The number of blanked pixels in Orion A and Orion B are 1475 and 1002 respectively. The final extinction maps constructed from the set of infrared extinctions are shown in Figure 3 and Figure 4. The median extinction values over the entire map for Orion A and Orion B are 2.1 and 2.2 magnitudes respectively. For both clouds, the extinction map resembles the basic outline of the ^{13}CO column density maps.

4   RESULTS

4.1   N(^{13}CO)A_v Relationship

Our analysis of near infrared stellar photometry from 2MASS and FCRAO molecular line data generates two inde-

pendent views of the mass distribution in the Orion molecular cloud. Dust extinction provides an excellent tracer of hydrogen column density, $N(H) = N(HI) + 2N(H_2)$, for a given line of sight based on the established relationships from UV spectroscopy, $N(H) = 5.8 \times 10^{21} E(B - V)$ cm^{-2}-mag^{-1} (Bohlin, Savage, & Drake 1978; Rachford et al. 2009) and $A_v/E(B - V) = 3.1$ (Whittet 2003). The H$_2$ column density is derived from the ^{13}CO column density with knowledge of the ^{13}CO abundance, N(H$_2$) = N(^{13}CO)/[^{13}CO/H$_2$]. However, the ^{13}CO abundance is expected to vary with the local environment conditions due to changing UV radiation field intensity, gas density structure, and chemical depletion.

Using the extinction as a reliable measure of the H$_2$ column density, we assess the ^{13}CO abundance by examining the relationship between N(^{13}CO) and A_v. The variations of ^{13}CO column density with A_v for the entire Orion A and Orion B clouds are displayed in Figure 6 as shaded 2 dimensional histograms within bins of A_v and N(^{13}CO). For the zoomed figures, the solid circles denote median values of N(^{13}CO) derived within varying sized bins of A_v which contain 250 points. The vertical and horizontal error bars reflect the standard deviation of N(^{13}CO) and A_v values respectively in each bin. Different trends are evident within three distinct regimes of extinction. Within the first regime at low A_v ($0 < A_v < 3$ mag), N(^{13}CO) grows very slowly with increasing A_v. The second extinction regime ($3 \leqslant A_v \leqslant 10$ mag) is characterized by much steeper linear growth of
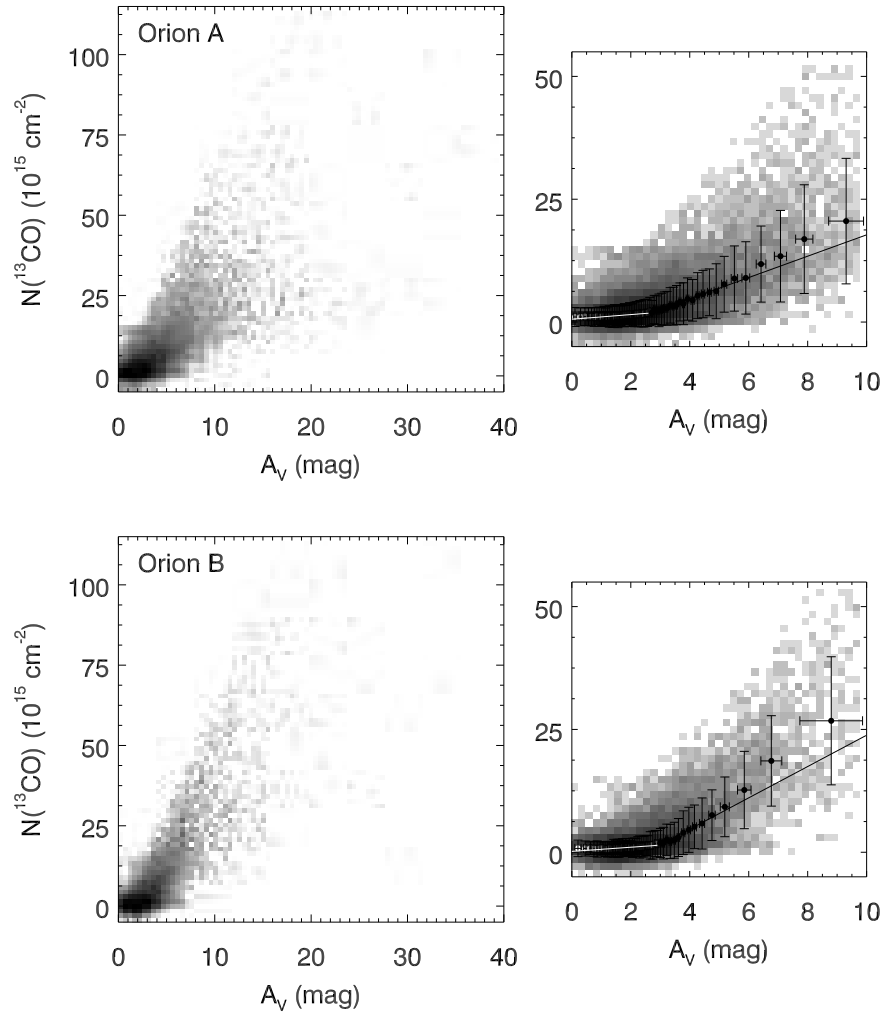
Figure 6. (left) 2D histograms showing the variation of $N(^{13}CO)$ with A_v for all defined pixels in the Orion A (top) and Orion B (bottom) clouds over the full range of visual extinction. (right) An enlarged version of the same figure over a more limited A_v range. The solid circles and vertical error bars represent the mean $N(^{13}CO)$ values and standard deviation respectively within equally populated A_v bins. Horizontal error bars show the dispersion of A_v values within each bin. The white and black solid lines show the fit of equation 7 for $A_v < A_{v,0}$ and equation 8 for $A_{v,0} < A_v < 10$ respectively.

$N(^{13}CO)$ with A_v. The third regime at high extinctions ($A_v > 10$ mag) shows a continued linear trend of $N(^{13}CO)$ but with a much larger scatter. For Orion A, the large scatter is due, in part, to a secondary set of points in which the ^{13}CO column density remains constant at the value $\sim 2.5 \times 10^{16}$ cm^{-2} with increasing A_v.

To quantify this transition from the low to intermediate A_v regime, a non-linear least squares (Levenberg-Marquardt) algorithm is applied to simultaneously fit two slopes (m_1 and m_2) and an intersection point ($A_{v,int}$,N_{int}) to the data over the range $0 < A_v \leqslant 10$ magnitudes,

$$N(^{13}CO) = m_1(A_v - A_{v,int}) + N_{int} \qquad (7)$$

for $0 < A_v < A_{v,int}$ and

$$N(^{13}CO) = m_2(A_v - A_{v,int}) + N_{int} \qquad (8)$$

for $A_{v,int} \leqslant A_v < 10$. This piecewise linear equation takes into account the significantly different $N(^{13}CO)$-A_v relationship of the first two regimes. The fitted parameters of equa-

tions 7 and 8 for Orion A and Orion B are listed in Table 1 and the fits are shown in Figure 6. These values describe the observed trends in Figure 6 in which $N(^{13}CO)/A_v$ ratio is small for $A_v < A_{v,int}$ and increases by factors of ~ 5 (Orion A) and ~ 8 (Orion B) for $A_v > A_{v,int}$.

The Orion A cloud offers a wide range of physical conditions (FUV radiation field, gas temperature, column density) that can impact the relation between $N(^{13}CO)$ and A_v. To assess the effect of the local environment on the $N(^{13}CO)$-A_v relation, we divide the cloud into 9 Galactic longitude partitions, each containing $\sim 2,500$ pixels of non-blanked data (see Figure 3). The Orion Nebula, M43, and NGC 1977 are located in partition 6 and make up part of the larger Orion OB1 Association that extends from partition 5 through partition 9. The $N(^{13}CO)$-A_v relation for each partition is shown in Figures 7-9. In these cases, the solid circles and error bars in the zoomed figures reflect the median and standard deviation respectively of $N(^{13}CO)$ values in A_v bins containing 50 points. The trends in the three A_v

Table 1. $N(^{13}CO) - A_v$ Relationship Fitted Parameters

Partition	m_1 (10^{15} cm^{-2} mag^{-1})	m_2 (10^{15} cm^{-2} mag^{-1})	$A_{v,int}$ (mag)	N_{int} (10^{15} cm^{-2})	$A_{v,3}$ (mag.)
Orion B	0.42 (0.05)	3.19 (0.20)	2.98 (0.05)	1.44 (0.07)	3.5 (0.1)
Orion A	0.47 (0.04)	2.17 (0.08)	2.68 (0.04)	1.84 (0.06)	3.2 (0.1)
1	0.4 (0.2)	1.5 (0.1)	2.7 (0.2)	3.0 (0.2)	2.7 (0.2)
2	0.7 (0.1)	2.3 (0.1)	2.7 (0.1)	2.7 (0.2)	2.8 (0.1)
3	0.4 (0.2)	1.8 (0.1)	2.2 (0.1)	2.0 (0.1)	2.8 (0.1)
4	0.5 (0.1)	4.4 (0.3)	3.2 (0.1)	2.4 (0.1)	3.3 (0.1)
5	0.8 (0.3)	2.0 (0.2)	2.3 (0.2)	2.2 (0.3)	2.7 (0.3)
6	0.5 (0.1)	3.6 (0.3)	3.7 (0.1)	2.1 (0.2)	4.0 (0.1)
7	0.3 (0.1)	1.7 (0.4)	3.1 (0.2)	1.2 (0.1)	4.2 (0.3)
8	0.1 (0.1)	0.9 (1.2)	2.9 (0.8)	0.9 (0.2)	5.2 (3.2)
9	-0.07 (0.1)	0.6 (0.5)	2.4 (0.3)	0.7 (0.1)	6.2 (3.2)
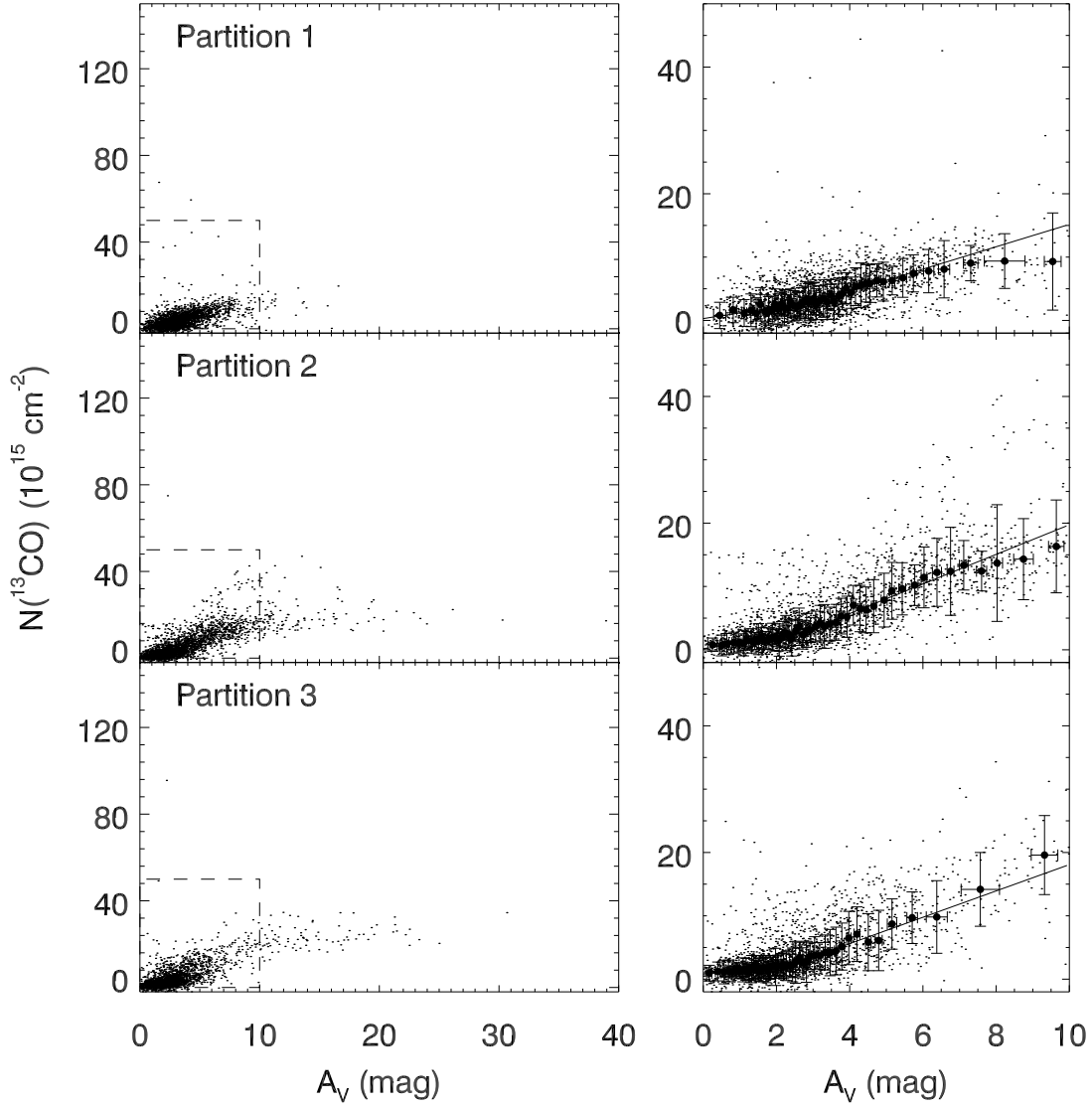
Figure 7. Same as Figure 6 for partitions 1 (top), 2 (middle), and 3 (bottom) of the Orion A cloud.

regimes observed in Figure 6 are evident in these localized regions of the cloud. For each partition, we fit Equations 7 and 8 to the 50 point A_v bins for $A_v \leqslant 10$ magnitudes. The results from these fits are summarized in Table 1.

The fitted slopes in the low A_v regime, m_1, are similar for partitions 1 through 6, ranging from 0.4-0.8×10^{15} cm^{-2} mag^{-1}. The northernmost partitions (7-9) show the lowest m_1 values, $< 0.3 \times 10^{15}$ cm^{-2} mag^{-1}. These values are consistent with little or no detected ^{13}CO in these areas. In the intermediate A_v regime, the slope, m_2, increases by a factor of 3 from partition 1 to partition 4. For partitions 4-6, the 2-line fit does not accurately describe the set of points in the range $5 < A_v < 10$ mag in which N(^{13}CO) values are in excess with respect to the fitted line. In these cases, the fitted parameters are leveraged by the large number of points between $A_{v,int}$ and 5 magnitudes with a lower ratio of N(^{13}CO) and A_v. For regions closer to the central region of the OB1 association (partitions 7-9), the slopes rapidly decrease. As noted in Section 3.1, the measured ^{13}CO column densities may be underestimated in the low volume density and low column density regions of the cloud owing to subthermal excitation of the J=1-0 transition. However, this error does not fully account for the measured differences between $m1$ and $m2$ over the expected conditions within the cloud responsible for detectable ^{13}CO emission.

The third A_v regime also shows differential behavior. In partitions 2-5, N(^{13}CO) does not continue to increase with increasing values of A_v above 12 mag. of visual extinction. However, in partition 6, N(^{13}CO) shows continued linear growth to visual extinctions of 30 mag. The different behavior in this partition accounts for the bifurcation of points in Figure 6 at high A_v values. Partitions 1,7,8, and 9 lack sufficiently high extinction to define the behavior of N(^{13}CO) in this regime.

4.2   The W_{CO}-A_v Relationship

Velocity-integrated ^{12}CO J=1-0 emission, W_{CO}, is the most frequently applied measure of H$_2$ column density and mass in galaxies owing to its brightness and correlation with other tracers of H$_2$ such as γ ray and dust emission in the Milky Way (Ade et al. 2011; Bloemen et al. 1986; Strong & Mattox 1996). Here, we assess the point-to-point relationship of W_{CO} with the infrared derived extinction in the Orion A and B clouds and within the Orion A partitions. Figure 10 displays the variation of W_{CO} with A_v over the surveyed areas of the Orion A and B clouds. As a convenient reference, the line corresponding to the standard conversion of W_{CO} to H$_2$ column density, $N_{H2} = 1.9 \times 10^{20} W_{CO}$ cm^{-2}/$(Kkms^{-1})$ and $N_{H2} = 9.4 \times 10^{20} A_v$ cm^{-2} is also drawn on the plots. As found in previous studies, W_{CO} correlates well with A_v over the limited extinction range of ∼2-5 magnitudes (Pineda, Caselli, & Goodman 2008; Pineda et al. 2010). Yet for a fixed value of A_v, there is a large scatter of W_{CO} values. This scatter limits the use of ^{12}CO emission as an accurate measure of the H$_2$ column density for a given line of sight through a molecular cloud. For extinctions less than 2 magnitudes, there is a large number of points below the reference line corresponding to weak or no detected signal of ^{12}CO emission. These points correspond to gas layers in which there is significant dust extinction but faint, underluminous ^{12}CO emission with respect

to typical ratios of W_{CO} to A_v. Since the derived A_v values are measured with respect to the extinction in the reference fields of background stars, the dust coupled to the atomic gas envelope has been largely removed. Most, if not all, of the extinction in the range of 0.1 to 2 magnitudes, is linked to dust associated with molecular hydrogen.

To better understand the origin of these various trends in the Orion clouds, we examine the W_{CO}-A_v relationship within different environmental conditions. Figure 11 shows this relationship within each partition of the Orion A cloud. In the lower partitions (1-5), W_{CO} linearly correlates with A_v between the range 1-5 magnitudes. For partitions 2 and 3, W_{CO} appears to saturate for $A_v > 5$. Pineda, Caselli, & Goodman (2008) find a similar trend in the subregions of the Perseus molecular cloud and attribute the flattening of W_{CO} with increasing A_v to high optical depths rather than depletion of ^{12}CO onto dust grains. In the areas closer to the OB association (partitions 6-9), there are many positions with A_v between 0 and 4 magnitudes for which CO emission is anomalously faint. These points correspond to underluminous locations noted in Figure 10 but can now be isolated within the cloud in the vicinity of the Orion OB stars.

5   DISCUSSION

In §4, we identify 3 distinct regimes in the relationship between the ^{13}CO column density and the infrared-derived visual extinction. In the following sections, we assume that the measured trends reflect the chemistry of ^{13}CO exposed to varying degrees of UV radiation with depth into the cloud, which in turn, depends on the local physical conditions of the cloud. The abundance of ^{13}CO relative to H$_2$ is calculated using the derived ^{13}CO column densities and dust extinction as a proxy of H$_2$ column density. These abundances are examined in the context of photochemistry models and the changing physical conditions within the Orion cloud. Line excitation and optical depth of the ^{13}CO J=1-0 line can also impact the observed N(^{13}CO)-A_v relationships. In regions of low volume density, $(n < 10^3$ cm$^{-3})$, that may characterize the low column density envelopes of GMCs, the J=1-0 transition is subthermally excited, $(T_{ex} <$ kinetic temperature) leading to weak emission that is difficult to detect in low sensitivity, wide field mapping programs such as the molecular line data presented in this study. In regions of high column density, $(A_v > 15$ mag.), the ^{13}CO J=1-0 emission may be optically thick and our method may not fully account for this effect. Our limited ^{12}CO and ^{13}CO J=1-0 data does not distinguish such excitation and opacity effects from chemical variations.

5.1   Baseline PDR Model

To illustrate our observational results, the Meudon PDR model is used to compute the variation of ^{13}CO abundances under varying physical conditions and UV radiation fields (Le Petit et al. 2006). The model describes the physical and chemical conditions within a slab of gas and dust with hydrogen density, n_H, and an incident FUV radiation field strength, χ, measured in units of the Draine (1978) radiation field. Although the model does not consider the de-
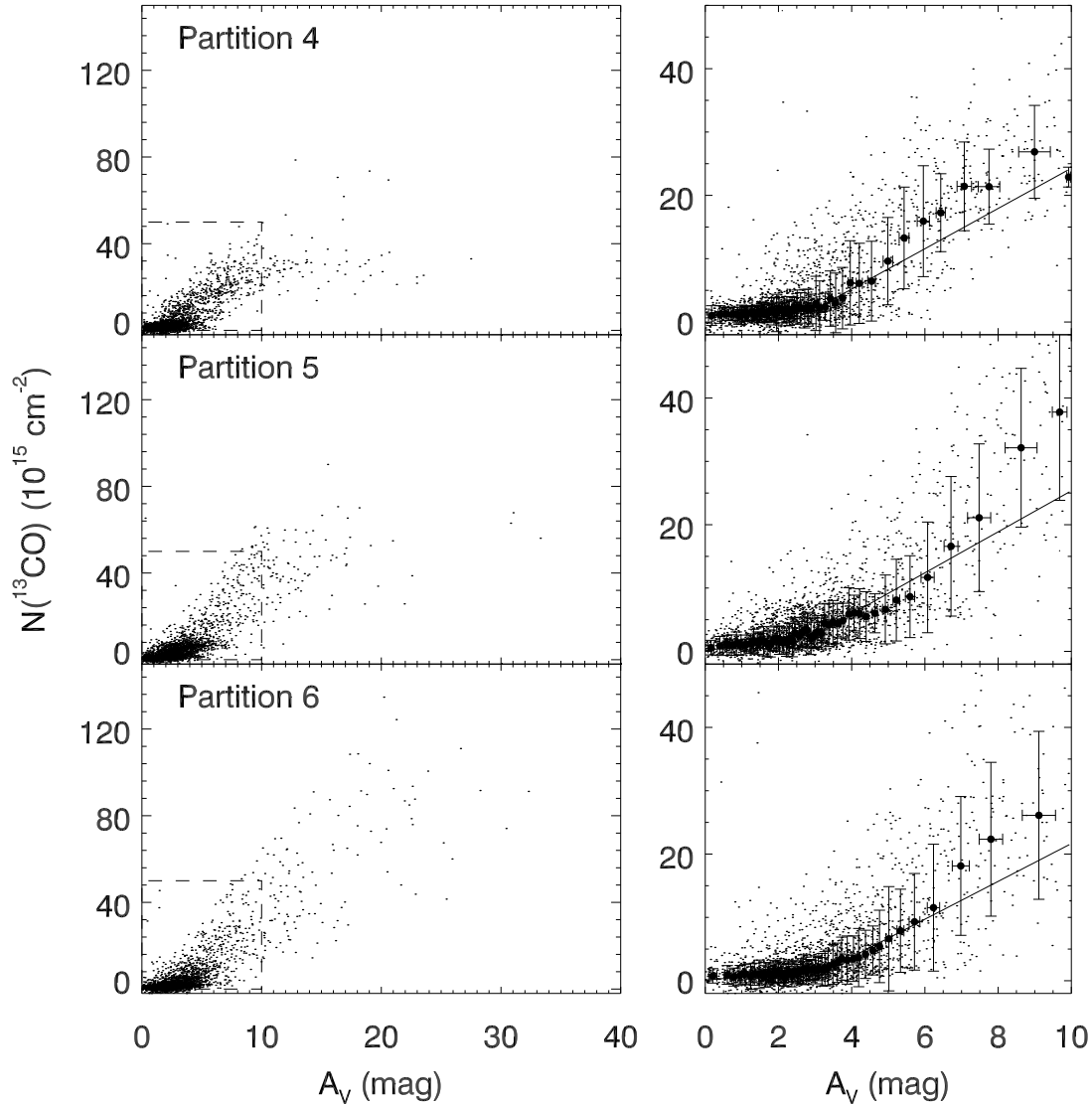
Figure 8. Same as Figure 6 for partitions 4 (top), 5 (middle), and 6 (bottom).

pletion of molecules onto grain surfaces at high densities, the photochemical calculation is sufficient for comparisons to data in the low to intermediate A_v regimes. The PDR models are calculated with parameters $\chi = 1, 10, 100, 10^3$, and 10^4 at a density of 10^3 cm^{-3} and $\chi = 10^3$ and 10^4 at a density of 10^4 cm^{-3}. These values of χ and volume density bracket the expected range of physical conditions throughout most of the Orion cloud as traced by ^{13}CO J=1-0 emission. For all model parameter sets, the UV radiation field is assumed to be incident on both sides of the slab. It is important to note when comparing the model results to the observations, that the model A_v values are measures of depth into the cloud with the corresponding ^{13}CO column density to each depth whereas the observed A_v and N(^{13}CO) values shown in Figures 6-9, reflect the total extinction and column density respectively through the cloud. For each depth position in the slab as measured by A_v, the model calculates

the fractional abundance of atomic and molecular hydrogen and selected molecules with respect to the total density of hydrogen protons, $n_H = n_{HI} + 2n_{H2}$.

The N(^{13}CO)-A_v relationships produced by the models with $n_H=10^3$ cm^{-3} are shown in Figure 12. These plots exhibit similar profiles as seen in Figures 6-9, for the low and intermediate A_v ranges — very small levels of ^{13}CO column density within the low A_v regime and a larger, yet constant value of N(^{13}CO)/A_v for the intermediate A_v regime. For a given volume density, the depth or equivalent, model A_v value above which the ^{13}CO abundance is constant, increases with increasing UV radiation field intensity (increasing χ). A higher radiation field strength requires a larger extinction to fully self-shield ^{13}CO molecules to achieve a maximum abundance. For cloud models with n=10^3 cm^{-3}, the depths at which 95% of the hydrogen is molecular are: A_v= 0.003, 0.12, 0.9, and 3.1 magnitudes for χ=1,10,100,1000 re-
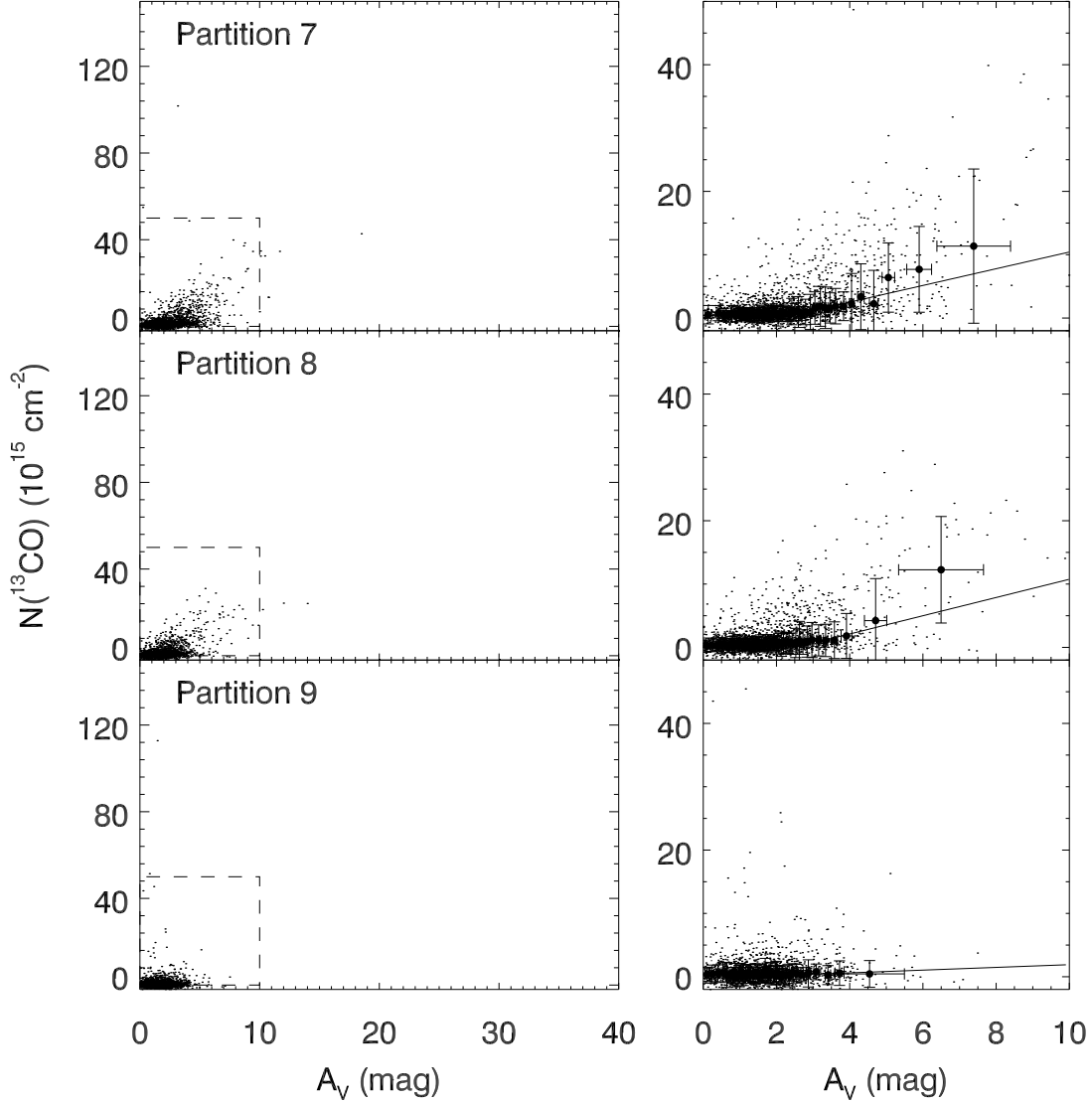
Figure 9. Same as Figure 6 for partitions 7 (top), 8 (middle), and 9 (bottom).

spectively. At these depths the ^{12}CO and ^{13}CO abundances are several orders of magnitude smaller than their nominal, strongly self-shielded values of 1×10^{-4} and 2×10^{-6} respectively. A consequence of the differential requirements for self-shielding of H_2, ^{12}CO and ^{13}CO is a layer of molecular hydrogen gas within the cloud envelope that is not traced by CO owing to its negligible abundance. This cloud component of molecular hydrogen with no CO has been labelled "dark" gas by Grenier et al. (2005) and may comprise a significant mass reservoir that must be considered when estimating the self-gravity and surface density of GMCs.

5.2 CO Abundance Variations from UV-Illuminated Cloud Envelope to the Self-Shielded Interior

The low extinction regime identified in our analysis represents areas within the cloud where the transition to fully self-shielded ^{13}CO material has not yet occurred such that photodissociation still dominates the chemistry of ^{13}CO. The shallow, non-zero slope, m_1, in this regime reflects the low effective abundance of ^{13}CO. To derive the mean relative abundance from these data, $[^{13}\text{CO}/\text{H}_2] = <\text{N}(^{13}\text{CO})/A_v/(\text{N}(H_2)/A_v> = m_1/9.4 \times 10^{20}$. The values range from $(1.1\text{-}8.5) \times 10^{-7}$ along the length of the Orion A cloud. The PDR models show that ^{13}CO abundance changes rapidly in this regime so these abundance estimates may not be representative of more narrow A_v intervals. The models
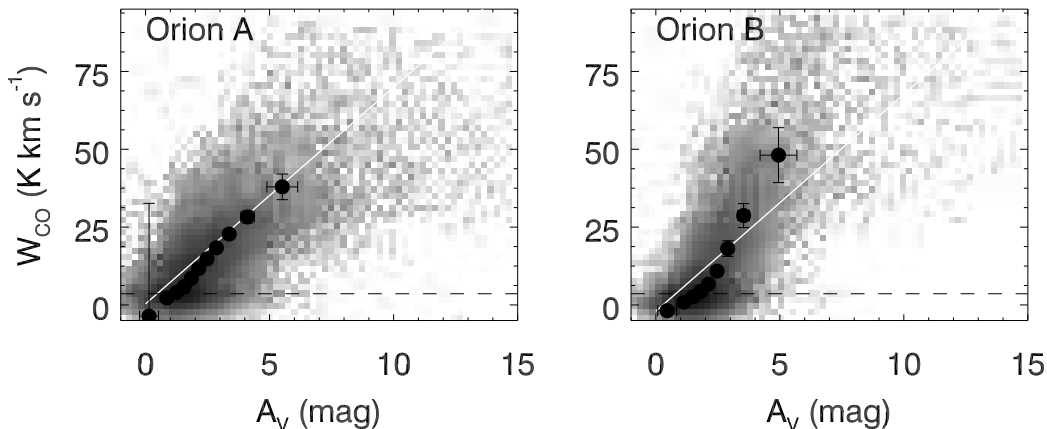
Figure 10. Two dimensional histograms of A_v and W_{CO} values for (left) Orion A and (right) Orion B. The solid circles and error bars reflect the mean and standard deviation within A_v bins containing 2048 individual points. The dashed horizontal line denotes the 3σ threshold of the W_{CO}. The white line shows the relationship implied by the standard conversion between W_{CO} and H_2 derived from γ-rays (Strong et al. 1996). For both clouds, W_{CO} is underluminous with respect to this standard value for $A_v < 2$ magnitudes.

show that there is an appreciable amount of H_2 mass within this layer.

At sufficient depths into the cloud, self-shielding enables the formation of appreciable column density of CO. In this self-shielded regime, a steeper slope, m_2 of the $N(^{13}CO)$-A_v relationship is measured, relative to slopes derived in the low A_v regime and reflects the increased abundance of ^{13}CO. Within this regime, the relative abundance is $[^{13}CO/H_2] = m_2/9.4 \times 10^{20}$. There are significant variations of the ^{13}CO abundance throughout the Orion A cloud. At the high longitude end of the cloud (partitions 1-3), the average abundance is 2.0×10^{-6}. In the central partitions of the cloud (partitions 4-6), the mean abundance increases to $\sim 3.5 \times 10^{-6}$. From this peak, the ^{13}CO abundances decrease in partitions 7 and 8. Finally, the measured slope in partition 9 is consistent with no appreciable ^{13}CO abundance.

These abundance results for the Orion A and Orion B molecular clouds are compared to values derived from other interstellar clouds with different conditions. Using V band star counts to estimate A_v towards 38 interstellar clouds, Dickman (1978) found a mean relative abundance of 2.0×10^{-6} with a scatter of 50% over the range $1.5 < A_v < 5$ magnitudes. With the availability of near infrared data to measure extinction in high column density regions, Frerking, Langer, & Wilson (1982) determined the ^{13}CO abundances of 1.5×10^{-6} ($1 < A_v < 5$) and 2.9×10^{-6} ($4 < A_v < 15$) for the Taurus and ρ-Oph molecular clouds respectively. For both Dickman (1978) and Frerking, Langer, & Wilson (1982), the abundance values are based on a limited number of positions in each cloud. The advent of large-scale, multiband near infrared observations enabled more spatially complete estimates of molecular abundances to deeper extinction regimes. Lada et al. (1994) investigated the dark cloud IC 5146 to A_v depths of 32 mag of extinction to derive a ^{13}CO abundance of 2.3×10^{-6}. More recent studies of the $N(^{13}CO)$-A_v relationship have analysed 2MASS data. Pineda, Caselli, & Goodman (2008) derived a mean ^{13}CO abundance of 2.5×10^{-6} for the Perseus molec-

ular cloud. Their study also found $\sim 25\%$ variations of the ^{13}CO abundance with the largest abundance values in the active star forming region, NGC 1333. Pineda et al. (2010) found a mean abundance of 1.6×10^{-6} in the Taurus molecular cloud. Harjunpaa, Lehtin, & Haikala (2004) examined a diverse set of molecular clouds to find a broad range of ^{13}CO abundances (0.9-3.5×10^{-6}) with the largest values linked to active star forming regions.

The conditions within the Orion A cloud span those found in both dark clouds as well as active star forming regions. The effective, global abundance of the Orion A cloud is similar to that of ρ Oph, which is a moderately active region of star formation containing a limited number of O and B stars. Partitions 1-3 are typical of quiescent star forming regions such as Taurus and IC 5146 and exhibit abundances similar to values found in these dark clouds. The abundances in the warmer, star-forming regions (partitions 4-6) of Orion A are more comparable to those found in active, star-forming regions. The partitions in Orion A show a similar trend as described in Harjunpaa, Lehtin, & Haikala (2004). The much lower abundances found in partitions 7 and 8 are likely a result of reduced extinction and a more intense UV radiation field. For partition 9, the second and third A_v regimes are non-existent, implying that the UV field intensity is too large for ^{13}CO to become self-shielded.

The elevated ^{13}CO abundance values in regions of active star forming regions within Orion and other targets pose an important constraint to descriptions of interstellar chemistry. Such enhanced abundances may result from the destruction of ice mantles on dust grains and the release of previously depleted CO molecules. Williams (1985) summarizes several mechanisms including the evaporation of the mantles from the energy released in radical reactions on the dust grains, photodesorption by UV radiation triggered by cosmic ray interactions with H_2 molecules in the interior of the cloud, and shocks generated from the interaction between dense clumps and stellar winds from young stellar objects.
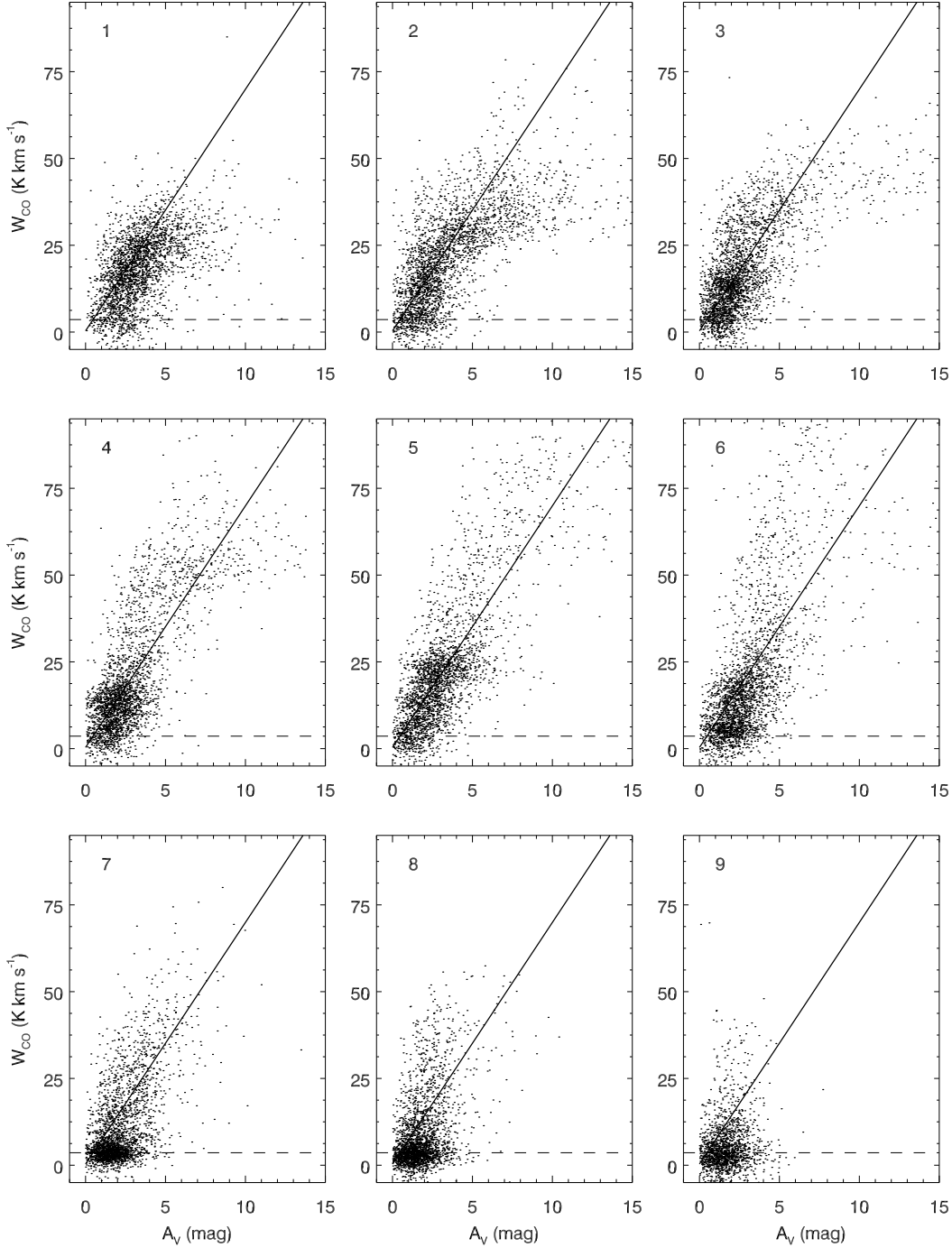
Figure 11. Scatter plots of the A_v and W_{CO} values for each Orion A partition. The line shows the relationship implied by the standard conversion between W_{CO} and H_2 and the dashed horizontal line denotes the 3σ threshold of the W_{CO}. The overdensity of points for $A_v < 3$ and $W_{CO} < 4$ K km s^{-1} in partitions 6-9 reflect underluminous ^{12}CO emission owing to reduced ^{12}CO abundance in this regime.

The transition of ^{13}CO abundances from the UV-illuminated envelope to the self-shielded interior are dependent on the physical conditions. To quantify this transition and enable a comparison of the data with models, we evaluate the A_v depth, $A_{v,3}$, at which $N(^{13}CO)$ equals a nominal yet significant value of 3×10^{15} cm^{-2}. For each partition in the Orion A cloud, $A_{v,3}$ is calculated from the parameters, m_2, $A_{v,int}$, and N_{int}. Figure 13 shows the variation of this

extinction threshold and model-derived thresholds for different values of χ/n. The extinction thresholds are not well characterized in partitions 8 and 9 owing to the absence of any significant ^{13}CO emission and therefore, are not included in this plot. $A_{v,3}$ is nearly constant at $\sim$2.7 mag. in partitions 1-3 and partition 5 and is well bounded by models with $0.001 < \chi/n < 0.005$. Given the large displacement of partitions 1-3 from the bright ionizing sources of the Orion
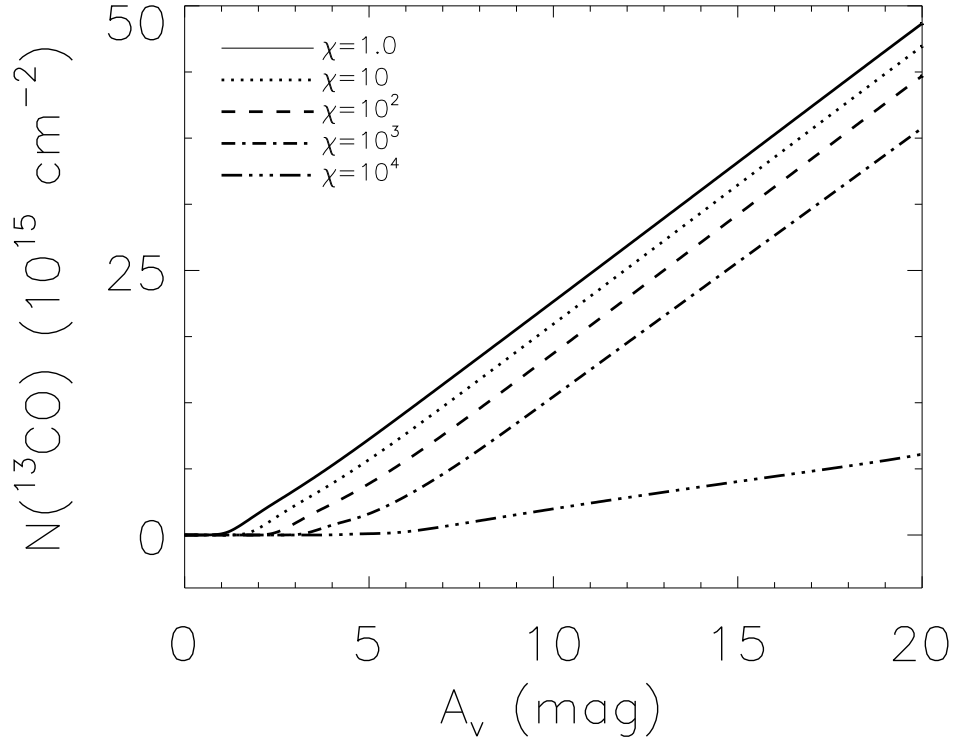
Figure 12. The relation between N(^{13}CO) and A_v derived from models produced by the Meudon PDR code for $n=10^3$ cm^{-3} and different values of the radiation field, χ (see legend). The model does not include the effects of ^{13}CO depletion onto dust grains.

OB association, we estimate the conditions $\chi \approx$ 1-5 and $n \approx 10^3$ cm^{-3} in these areas. Partition 5 lies closer to the OB association so one might expect an enhanced UV field but this could be balanced by a corresponding increase in the gas density. For partitions 6 and 7, $A_{v,3}$ increases to 4 magnitudes and is well matched with model values with χ/n of $\sim$0.1. This condition can be reasonably matched to $\chi=10^3$ and $n=10^4$ cm^{-3}. The absence of significant ^{13}CO emission in partitions 8 and 9, which lie near the centre of the OB association, likely indicates a very intense ultraviolet radiation field and a low density medium for which the condition for ^{13}CO self-shielding is not possible. The measured changes in the threshold extinctions in the various partitions reflect the varying intensity of the far ultraviolet radiation field owing to displacement from the Orion OB1 association and Orion Nebula Cluster and the local volume density conditions within the cloud.

5.3 High A_v Regime

The role of depletion of molecules onto interstellar dust grains in cold, high density regions of molecular clouds has been increasingly recognized owing to the availability of secondary tracers of H$_2$ column density that probe deep into the cloud, such as infrared derived extinction and submillimeter thermal dust continuum emission. Lada et al. (1994) observed a flattening of ^{13}CO integrated intensity

in the IC 5146 cloud for lines of sight with $A_v >$ 8-10 magnitudes. Kramer et al. (1999) found a similar trend in IC 5146 for C^{18}O column densities for $A_v >$ 10, which they attributed to depletion. Other examples of depletion include the globule B68 (Bergin et al. 2002), starless cores (Tafalla et al. 2002), filaments within the Taurus cloud (Pineda et al. 2010). Christie et al. (2012) examined depletion effects in a sample dust cores within several Gould's Belt clouds, including regions in Orion B. They found depletion of C^{18}O to be most severe in the Taurus cloud and smallest in the Ophiuchus cloud. Both prestellar and protostellar cores within the Orion B cloud exhibit varying degrees of C^{18}O depletion.

Models of molecular cloud chemistry that consider depletion identify several key factors that modulate molecular abundances. Bergin, Langer, & Goldsmith (1995) show depletion of CO depends strongly on dust temperature, density, and timescale. At low densities ($<10^4$ cm^{-3}) and extinctions, the effect of depletion is small owing to desorption by cosmic rays and radiation that maintain significant fractions (60-90%) of CO in the gas phase, even at late times of 10^7 years. For densities in excess of 10^5 cm^{-3}, dust temperatures of 10 K, and $A_v=$10 mag., the depletion time scales are short and much of the CO ($\sim$96%) freezes onto the grain surfaces. For increasing grain temperature, molecules attached to grain surfaces are released by thermal evaporation of the grain mantles. Bergin, Langer, & Goldsmith (1995) show
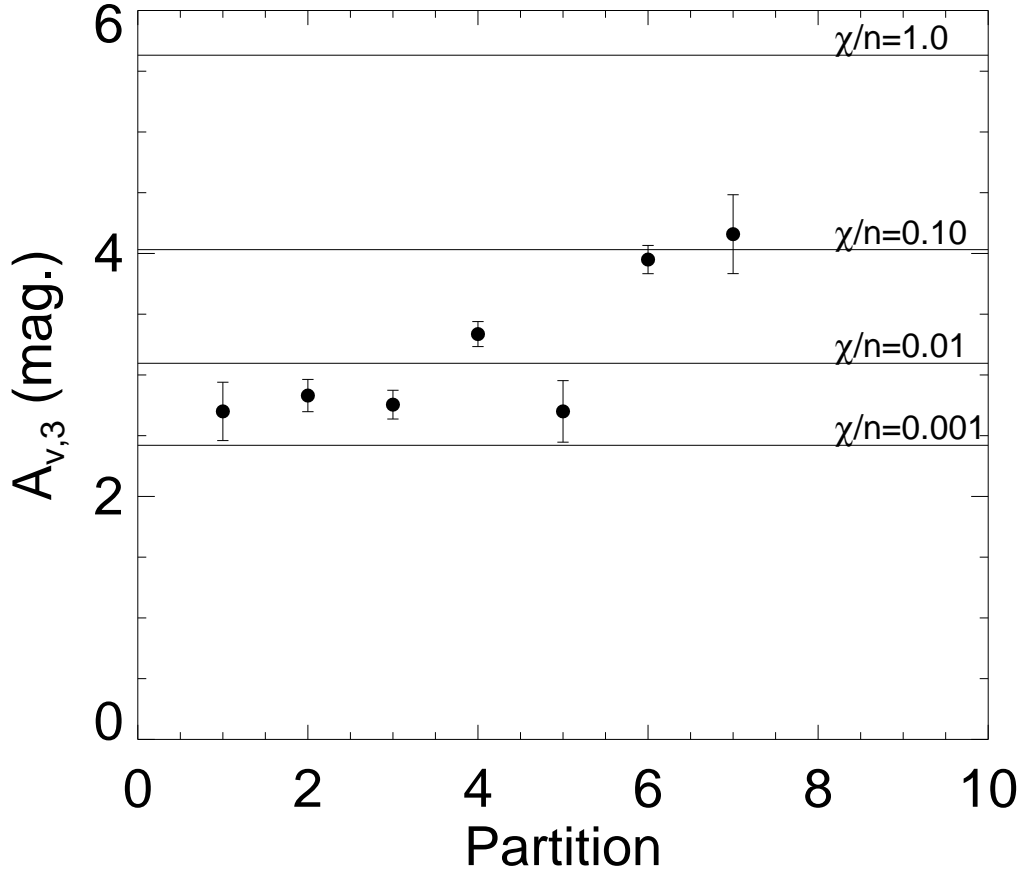
Figure 13. Values of the extinction, $A_{v,3}$, at which $N(^{13}CO) = 3 \times 10^{15}$ cm^{-2} for partitions 1-7 in the Orion A cloud. The horizontal lines correspond to $A_{v,3}$ calculated for each PDR model described by different values of χ/n. The variation of $A_{v,3}$) in the cloud is linked to proximity to the Orion OB association and changes in the local volume density of the gas.

that thermal evaporation is an extremely effective desorption process at dust temperatures greater than 22 K with the degree of chemical depletion depending on the effectiveness of the desorption processes. For temperatures larger than $\sim$25 K the models calculate that all CO is expected to be found in the gas phase However, temperature programmed desorption (TPD) laboratory studies demonstrate that CO molecules can be locked into water ice on grain mantles and that CO remains partially (25-40%) depleted on these surfaces to even higher temperatures (Collings et al. 2004).

In the Orion A cloud, differential behavior in the high A_v regime is identified. In partitions 2-5, the extinction at which the $N(^{13}CO)$-A_v relation flattens represents the depth at which environmental conditions are appropriate for ^{13}CO depletion onto dust grains. The turn-over occurs at approximately 10 mag in partitions 2-4 and 15 mag in partition 5. In contrast, partition 6 shows continued linear growth with increasing A_v above 10 mag. Owing to the limited range of A_v in partitions 1,7,8, and 9, it is not possible to assess the role of depletion in these areas.

To examine the role of temperature in the depletion process, the gas temperatures derived from the optically thick CO emission in each partition are examined as a proxy or

relative measure to the grain temperature, considered in the models. Table 2 shows the mean excitation temperatures T_{ex} for two regimes of extinction, moderate ($5 < A_v < 10$) and high ($A_v > 10$), chosen to ensure that the CO lines are thermalized and to sample the high column density regions where depletion occurs. The temperature within the high extinction regions of partitions 2-4 are all below the 22 K threshold calculated in the models, while partition 5 reaches 25 K. In partition 6, where the temperatures are significantly higher ($T_{ex} = 34.0$ K), a significant fraction of ^{13}CO remains in the gas phase to A_v=25 magnitudes. The limited amount of depletion in Partition 6 may also explain why it has the largest CO abundance in the cloud. Our data can not assess whether a significant amount of CO remains entrapped in water ice as measured in the TPD studies. If a large amount (50%) of CO remains depleted in these regions, as measured in the TPD experiments, then the interstellar abundance of CO is much larger than conventionally assumed.

Thus, CO depletion is observed in the cold, dense regions of the Orion A cloud. The scatter and bifurcation of the Orion A composite $N(^{13}CO)$-A_v relation shown in Figure 6 is attributed to varying conditions within the cloud that allow chemical depletion of ^{13}CO onto dust grains in

Table 2. Properties within Partitions

	T_{ex}^a (K)	T_{ex}^b (K)	M_H (M$_\odot$)	M_{HI} (M$_\odot$)	$M_{H2,U}$ (M$_\odot$)	$M_{H2,SS}$ (M$_\odot$)	$M_{LTE,U}$ (M$_\odot$)	$M_{LTE,SS}$ (M$_\odot$)	L$_{CO,U}$ (Kkms^{-1}pc^2)	L$_{CO,SS}$ (Kkms^{-1}pc^2)	M/L_{CO} (M$_\odot$/Kkms^{-1}pc^2)
Orion B	16.9	22.6	46300	4800	21900	19600	10000	24500	6100	8400	2.9
Orion A	19.2	26.3	63100	3000	23800	36200	15000	36200	7900	10800	3.2
1	12.6	12.9	8100	300	1600	6200	1400	4300	600	1600	3.6
2	14.3	15.8	9600	200	2000	7400	1600	6800	800	2000	3.4
3	15.3	16.9	7500	300	2300	4900	1900	4300	900	1300	3.2
4	19.6	21.3	7800	300	3000	4500	2200	5600	1100	1500	2.8
5	19.3	25.7	8500	300	1900	6300	1500	7400	800	2100	2.8
6	21.4	33.0	9300	600	3700	5000	2000	6900	1200	1900	2.8
7	19.7	23.5	5400	500	3800	1200	1800	900	1000	300	3.6
8	15.0	21.4	4300	400	3700	300	1600	300	1000	100	3.8
9	7.3	——	2600	100	2500	13	900	10	400	1	5.8

a: For $5 < A_v < 10$ mag

b: For $A_v > 10$ mag

the cold, dense regions and desorb ^{13}CO molecules in the warmer regions of the cloud.

5.4 Cloud Masses

An important goal of this study is to assess the reliability of ^{12}CO and ^{13}CO J=1-0 emission as a tracer of H$_2$ mass within interstellar clouds under varying physical conditions. This effort is critical to studies of the molecular ISM and star formation throughout the Milky Way and within nearby galaxies, where infrared-derived extinctions over the angular extent of GMCs are not possible. Previous calibrations of the ^{13}CO abundance in cold, dark clouds may not apply to the more massive GMCs that contribute the bulk of the CO luminosity in galaxies. The global masses of the Orion A and B clouds and the masses within the individual partitions of Orion A are calculated for different cloud layers using the derived A_v distributions, HI 21 cm line emission, ^{12}CO and ^{13}CO J=1-0 emission. For the atomic gas component, we analyse the 21 cm line emission from the Atlas of Galactic Neutral Hydrogen (Hartmann & Burton 1997). For all mass calculations, we exclude positions for which the extinction is not defined in the high A_v regions, contain no CO data or have statistical errors for the ^{13}CO column density in excess of 5×10^{16} cm^{-2}. Such regions account for 5.4% and 1.6% of the respective areas in Orion A and Orion B. For a given position on the sky, $\mathbf{r}$, the total hydrogen column density, $N_H(\mathbf{r}) = N_{HI}(\mathbf{r}) + 2N_{H2}(\mathbf{r})$, is derived from the infrared-derived extinction using the conversion, $N_H(\mathbf{r}) = 1.88\times10^{21} A_v(\mathbf{r})$ cm^{-2} (Rachford et al. 2009). The total mass of the surveyed area is

$$M_{\rm H} = \mu m_{\rm H} D^2 \int_{cloud} d\Omega N_H(\mathbf{r}) \qquad (9)$$

where $m_{\rm H}$ is the mass of the hydogen atom, μ is the mean atomic weight to account for helium (1.36), D is the distance to the cloud (410 pc for Orion), and $d\Omega$ corresponds to the solid angle of an image pixel. The atomic gas column density for each position is determined from the velocity integrated HI 21 cm line brightness temperature, $T_{21}(\mathbf{r},v)$,

$$N_{HI}(\mathbf{r}) = 1.82 \times 10^{18} \left[\int dv T_{21}(\mathbf{r},v) \right] - N_{HI,ref} \quad \text{cm}^{-2} (10)$$

where $N_{HI,ref} = 1.1 \times 10^{21}$ cm^{-2} is the atomic gas column density derived from the HI 21 cm line within the reference fields used to establish the mean colours of background stars in the calculation of A_v. Therefore, the column densities and masses derived from A_v and the HI 21 cm line emission are relative to column density values in these reference fields. The HI 21 cm line emission is integrated over the velocity interval -5 to 21 km s^{-1} to account for the more extended velocity dispersion of the atomic gas relative to the molecular component. The equivalent extinction of this HI column density is $A_{v,HI} = N_{HI}/1.88 \times 10^{21}$ magnitudes. The corresponding mass of atomic gas, including helium, is

$$M_{\rm HI} = \mu m_{\rm H} D^2 \int_{cloud} d\Omega N_{HI}(\mathbf{r}) \qquad (11)$$

For the molecular gas, two components of the mass are derived from the visual extinction. The first component is determined within the low A_v regime by considering only those lines of sight with extinctions in the range, $A_{v,HI} < A_v < A_{v,3}$, corresponding to where ^{13}CO is underabundant. The molecular hydrogen mass within this regime, $M_{H2,U}$, is

$$M_{H2,U} = \mu m_{\rm H} D^2 \left[1.88\times10^{21} \int d\Omega A v(\mathbf{r}) - \int d\Omega N_{HI}(\mathbf{r}) \right] (12)$$

for $A_{v,HI} < A_v < A_{v,3}$. The second mass component, $M_{H2,SS}$,

$$M_{H2,SS} = \mu m_{\rm H} D^2 \left[1.88\times10^{21} \int d\Omega A v(\mathbf{r}) - \int d\Omega N_{HI}(\mathbf{r}) \right] (13)$$

for $A_v > A_{v,3}$, corresponds to the mass within the strongly self-shielded layers of the cloud. Owing to the large difference between the beam size of the HHI 21 cm line observations (36$'$) and the pixel size of the extinction maps (1.8$'$), we assume a smooth distribution of the atomic gas column density between these angular scales.

The molecular hydrogen mass is also estimated from the distribution of ^{13}CO column density. Traditionally, one assumes a constant value of the ^{13}CO to H$_2$ abundance ratio throughout the cloud. Here, we assess the errors in the ^{13}CO derived mass, M_{LTE} using the standard ^{13}CO to H$_2$ abundance 2×10^{-6} (Dickman 1978) that is typically applied in studies of GMCs (Carpenter, Snell, & Schloerb 1995; Heyer et al. 2009) and compare the result to the A_v

derived values in both the underabundant and strongly self-shielded regimes.

$$M_{LTE,U} = \mu m_{H2} D^2 (5 \times 10^5) \int d\Omega N(^{13}CO)(\mathbf{r}) \qquad (14)$$

for $A_{v,HI} < A_v < A_{v,3}$ and

$$M_{LTE,SS} = \mu m_{H2} D^2 (5 \times 10^5) \int d\Omega N(^{13}CO)(\mathbf{r}) \qquad (15)$$

for $A_v > A_{v,3}$. Finally, we calculate the ^{12}CO luminosity in each cloud and partition for each A_v regime,

$$L_{CO,U} = D^2 \int d\Omega \int dv T_{12,mb}(\mathbf{r}, v) \qquad (16)$$

for $A_{v,HI} < A_v < A_{v,3}$ and

$$L_{CO,SS} = D^2 \int d\Omega \int dv T_{12,mb}(\mathbf{r}, v) \qquad (17)$$

for $A_v > A_{v,3}$. $T_{12,mb}(\mathbf{r}, v)$ is the ^{12}CO spectrum for position, $\mathbf{r}$ within the map. The derived masses for the Orion A and B clouds and the Orion A partitions are listed in Table 2. The corresponding CO luminosity to molecular mass conversion factor, $M/L_{CO} = (M_{H2,U} + M_{H2,SS})/(L_{CO,U} + L_{CO,SS})$ is also calculated.

The atomic masses listed in Table 2 are limited to the area covered by the CO observations and derived from atomic gas column densities from which $N_{HI,ref}$ has been subtracted. The residual masses reflect the amount of atomic material that resides within the foreground and background layers of the Orion molecular cloud as well as the small component of atomic hydrogen expected to be present within the deep, strongly self-shielded interior of the cloud owing to cosmic rays (Goldsmith & Li 2005). For the lines of sight in the vicinity of the molecular cloud over the limited area shown in Figures 1 and 2, this residual atomic gas provides a small contribution (2-10%) to the total hydrogen column density. However, if one were to restore the layer of atomic gas represented by $N_{HI,ref}$, the mass of atomic gas in the observed CO area increases to 1.7×10^4 M$_\odot$ for Orion A and and 2.0×10^4 M$_\odot$ for Orion B. Moreover, the atomic envelope of the Orion cloud extends well beyond the surveyed area so the total atomic mass of the Orion region is likely much larger than these calculated values. Grenier et al. (2005) tabulated the gas masses in the Orion cloud over a much larger area and found a ratio of ^{12}CO derived molecular to atomic gas mass of 1.2:1 that indicates an extended component of atomic gas well beyond the surveyed areas of Figures 1 and 2.

Inspection of Table 2 shows that the ^{13}CO LTE column density with a constant ^{13}CO to H$_2$ abundance of 2×10^{-6} provides a reasonably accurate measure of the H$_2$ mass residing within the self-shielded interiors of the Orion cloud despite the large abundance variations within the cloud. In this regime, the ^{13}CO mass slightly overestimates the mass determined by extinction by 25% in Orion B. In Orion A, the respective masses are identical. The root mean square deviation is 23% for the 9 paritions in Orion A with a maximum deviation of 40% occuring within Partition 6, which also exhibits an enhanced ^{13}CO to H$_2$ abundance ratio. The self-shielded layer of the cloud is critical to the star formation process as it is the substrate from which dense filaments and cores develop and from which newborn stars emerge.

However, this self-shielded zone comprises a fraction of the total molecular mass of the cloud – 60% in Orion A and 47% in Orion B.

The ^{13}CO derived masses with a constant abundance systematically underestimate the H$_2$ mass within the low A_v, ^{13}CO underabundant regime by factors as large as 3. Figure 14 shows a cumulative histogram of the inferred H$_2$ mass, respectively traced by the infrared-derived A_v and ^{13}CO, which resides within varying zones of visual extinction For each cloud approximately 50% of the H$_2$ mass resides within lines of sight with $A_v < A_{v,3}$ in which the ^{13}CO abundance is low and changing rapidly. While the small opacity of the low J transitions of ^{13}CO are appealing to discern cloud structure and kinematics (Goldsmith et al. 2008; Heyer et al. 2009), investigators must recognize that these emission lines are insensitive to the more extended reservoir of molecular gas that may comprise a significant fraction of the cloud mass. In regions of high UV radiation such as partitions 7-9 in Orion A, this missing fraction can be even larger.

Dark gas describes the low A_v regime in the vicinity of molecular clouds in which molecular hydrogen is abundant due to efficient self-shielding but the abundance of ^{12}CO is low (Grenier et al. 2005; Wolfire & McKee 2010). In these conditions, ^{12}CO is underluminous with respect to its standard relationship with H$_2$ at moderate values of A_v. In the A_v range to which our maps are sensitive, there is little evidence for dark gas throughout most of the Orion A and Orion B clouds. The M/L_{CO} ratios in the underluminous regime are comparable to those derived in the strongly, self-shielded regions. Dark gas is more evident in Orion A partitions 7-9 where the M/L_{CO} ratios are larger than the values in the self-shielded regime. In these regions, the UV field is enhanced by the UV emitting young stars of the OB association as illustrated in Figure 11 allowing for the destruction of CO molecules while maintaining a large fraction of molecular hydrogen gas.

The conversion factor, X_{CO}, relates the integrated ^{12}CO emission, W_{CO}, to the column density of H$_2$ molecules, $N_{H2} = X_{CO} W_{CO}$. The use of the optically thick ^{12}CO line as a tracer of column density has been justified by both simple models of interstellar clouds (Dickman, Snell, & Schloerb 1986) and more recently, by computational simulations that include molecular chemistry (Glover & Mac Low 2011; Narayanan et al. 2012).

Digel, Hunter, & Mukherjee (1995) and Digel et al. (1999) studied the X_{CO} factor specifically within the Orion molecular cloud using >100 MeV γ-rays, ^{12}CO and HI 21 cm line emission spanning a much larger area than the more limited imaging shown in Figures 1 and 2. They found $X_{CO} = 1.35 \times 10^{20}$ cm^{-2}/(K km s^{-1}) corresponding to a M/L_{CO} ratio of 2.9 M$_\odot$/(K km s^{-1} pc^2). This conversion includes contributions from helium atoms to the mass budget. The Orion X_{CO} value is lower than the Galactic mean using γ-rays (Strong & Mattox 1996) and much lower than a recent determination using dust emission from clouds in the solar neighborhood (Ade et al. 2011). This gamma-ray derived value of X_{CO} is similar to those calculated for Orion A (3.2) and Orion B (2.9) in Table 2 using our ^{12}CO measurements and A_v.

More recently, the Orion cloud complex was observed by the Fermi Large Area Telescope (Ackermann et al. 2012). This study found a difference in X_{CO} values between the
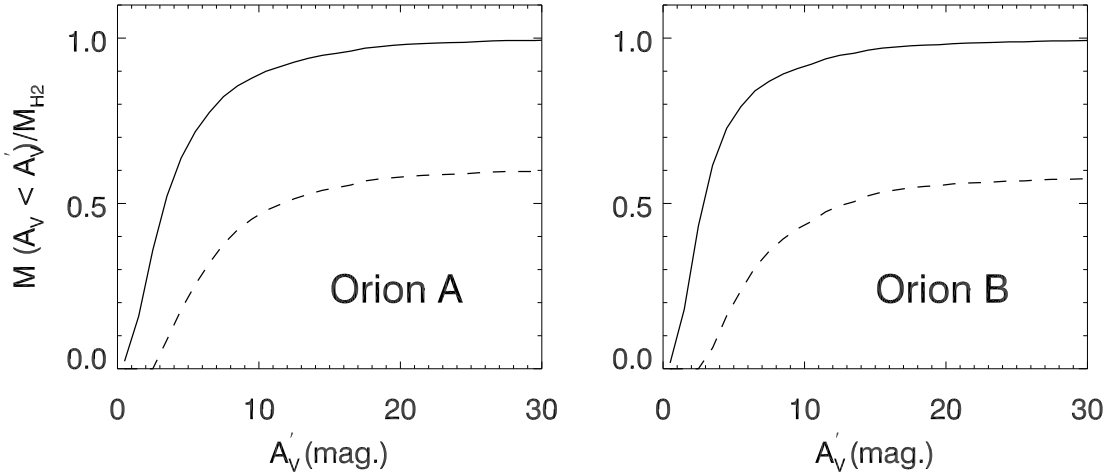
Figure 14. A cumulative histogram of molecular mass in Orion A and Orion B for $A_v < A_v'$ as traced by A_v (solid line), ^{12}CO, (dashed-dotted line) assuming a CO luminosity-to-mass factor tabulated for each cloud in Table 2, and N(^{13}CO) (dashed line) with an ^{13}CO-to-H$_2$ abundance of 2.0×10^{-6}. 50% of the H$_2$ masses reside within the low A_v regimes of the clouds.

high longitude end of the Orion A cloud ($l > 212$) where $X_{CO} = 2.3 \times 10^{20}$ cm^{-2}/(K km s^{-1}) (M/L_{CO}=4.9) and the remainder of the Orion A cloud as well as Orion B where $X_{CO} = 1.3 \times 10^{20}$ cm^{-2}/(K km s^{-1}) (M/L_{CO}=2.8). They attribute these differences to the rapid changing CO abundance in the diffuse gas regime at high longitudes of the Orion cloud and the larger contribution by "dark" H$_2$ material to the total molecular mass. While our observations do not extend as far as the gamma ray imagery, we derive an elevated mass weighted average M/L_{CO} of 3.5 M$_\odot$/(Kkms^{-1}pc^2) within partitions 1 and 2 for which $l > 212$ compared to the remainder of the Orion A cloud where M/L_{CO}=3.1 M$_\odot$/(Kkms^{-1}pc^2). We also note the high values of M/L_{CO} in partitions 7,8,9 that are close to the central region of the OB associaton and illuminated by local UV radiation fields.

Our estimates of X_{CO} in Orion are smaller than the value (2.8×10^{20} cm^{-2}/(K kms^{-1})) derived by Paradis et al. (2012) that is also based on infrared extinctions using 2MASS. Paradis et al. (2012) examined a more extended area than that shown in Figures 1 and 2 and employed a different algorithm (Dobashi 2011) to account for foreground star contamination, which may account for the measured differences.

Our results for the Orion molecular cloud and those derived from gamma ray measurements emphasize that there are large variations of X_{CO} in the interstellar medium. The application of the Galactic averaged value to an individual cloud can lead to 100% errors in the molecular mass. Moreover, the scatter in the W_{CO}-A_v relationship (see Figures 10 and 11) demonstrate that the varying environments within a molecular cloud can lead to even larger errors in the H$_2$ column density.

6 CONCLUSIONS

In this study, we derive two independent views of the molecular mass distribution in the Orion A and Orion B molecular clouds using ^{12}CO and ^{13}CO line emission and IR stellar photometry from 2MASS. These data are analysed to investigate the variation of ^{13}CO abundances over the changing physical conditions within the cloud and to evaluate the effectiveness of ^{13}CO emission as tracer of molecular mass in interstellar clouds. We find the following results.

• Three distinct regimes are identified in the N(^{13}CO)-A_v relationship: the photon-dominated envelope at $A_v < 3$ mag., the fully self-shielded cloud interior at $3 < A_v < 10$ mag. in which the ^{13}CO abundance is stable, and high column density zones ($A_v > 10$ mag.) in which CO can deplete onto cold dust grains. The degree to which each regime is present depends on the local physical conditions – in particular, the strength of the UV radiation field and the temperature of dust grains.

• In Orion A, the measured depth of the PDR envelope increases with proximity to the centre of the Orion OB1 association, which provides the primary source of UV radiation. This spatial dependence emphasizes the requirement of a self-shielding layer to develop significant ^{13}CO abundance values. The relative ^{13}CO abundance within the fully, self-shielded regime varies across the cloud from a minimum of 1.4×10^{-6} to 3.4×10^{-6}. The maximum ^{13}CO abundance occurs near the Orion Nebula Cluster.

• The presence of CO depletion onto dust grains depends on the local gas temperature that serves as a relative measure of the dust temperature. The observed dependence points to the role of thermal evaporation of CO molecules from grain surfaces whose temperature is above a critical value. The regions closer to the Orion OB1 association show less depletion, which may account for the higher ^{13}CO abundances found there.

• Assuming a constant ^{13}CO to H$_2$ abundance of 2×10^{-6} throughout the cloud, the ^{13}CO, LTE derived column densities provide an accurate accounting of the H$_2$ mass in layers of the cloud that are fully self-shielded. In Orion, this layer comprises ∼50% of the total molecular mass of the cloud.

• Using dust extinction as a measure of H$_2$ column den-

sity, we confirm the reduced value of X_{CO} in Orion relative to the Galactic mean value previously derived from gamma-ray measurements. This difference attests to variations of X_{CO} in the interstellar medium.

REFERENCES

Ackermann, M. et al. 2012, ApJ, 756, 4

Ade, P.A.R et al. 2011, AA, 536, 19

Alves, J., Lada, C. J., & Lada, E. A. 1999, ApJ, 515, 265

Bally, J., Langer, W.D., & Liu, W. 1991, ApJ, 383, 645

Bergin, E. A., Alves, J., Huard, T., & Lada, C. J. 2002, ApJ, 570, L101

Bergin, E. A., Langer, W. D., & Goldsmith, P. F. 1995, ApJ, 441, 222

Bloemen, J. B. G. M., Strong, A. W., Mayer-Hasselwander, H. A., Blitz, L., Cohen, R. S., Dame, T. M., Grabelsky, D. A., Thaddeus, P., Hermsen, W., Lebrun, F. 1986, AA, 154, 25

Bohlin, R. C., Savage, B. D., & Drake, J. F. 1978, ApJ, 224, 132

Buckle, J.V., Hills, R.E., Smith, H., et al. 2009, MNRAS, 399, 1026

Buckle, J.V., Davis, C.J., DiFrancesco, J. et al. 2012, MNRAS, 422, 521

Carpenter, J. M., Snell, R. L., & Schloerb, F. P. 1995, ApJ, 445, 246

Charnley, S. B., Dyson, J. E., Hartquist, T. W., & Williams, D. A. 1988 MNRAS, 231, 269

Christie, H., Viti, S., Yates, J., Hatchell, J. Fuller, G.A. et al. 2012, MNRAS, 422, 968

Collings, M.P., Dever, J.W., Fraser, H.J., McCoustra, M.R.S., Williams, D.A. ApJ, 583, 1058

Dame, T.M., Hartmann, D. & Thaddeus, P. 2001, ApJ, 547, 792

Dickman, R. L. 1978, ApJS, 37, 407

Dickman, R. L., Snell, R. L., & Schloerb F. P. ApJ, 309, 326

Digel, S.W., Aprile, E., Hunter, S. D., Mukherjee, R., & Xu, F. 1999, ApJ, 520, 196

Digel, S.W., Aprile, E., Hunter, S. D., Mukherjee, R., & Xu, F. 1999, ApJ, 520, 196

Dobashi, K. 2011, PASJ, 63, 1

Draine, B. T. 1978, ApJS, 36, 595

Duvert, G., Cernicharo, J., & Baudry, A. 1986, AA, 164, 349

Erickson, N. R.. Grosslein, R. M., Erickson, R. B., & Weinreb, S. 1999, IEEE Trans. Microwave Theory Tech., 47(12), 2212

Evans, II, N. J., Rawlings, J. M. C., Shirley, Y. L., & Mundy, L. G. 2001, ApJ, 557, 193

Frerking, M. A., Langer, W. D., & Wilson, R. W. 1982, ApJ, 262, 590

Glover, S.C.O. & Mac Low, M.-M. 2011, MNRAS, 412, 337

Goldsmith, P.F. & Li, D. 2005, ApJ, 622, 938

Goldsmith, P.F., Heyer, M., Narayanan, G., Snell, R.L., Li, D., & Brunt, C. 2008, ApJ, 680, 428

Grenier, I.A., Casandjian, J-M., & Terrier, R. 2005, Science, 307, 1292

Harjunpaa, P., Lehtinen, K., & Haikala, L. K. 2004, AA, 421, 1087

Hartmann, D. & Burton, B.W. 1997, Atlas of Galactic Neutral Hydrogen, Cambridge University Press

Heyer, M., Krawczyk, C., Duval, J., & Jackson, J. M. 2009, ApJ, 699, 1092

Hollenbach, D. J. & Salpeter, E. E. 1971, ApJ, 163, 155

Hollenbach, D. J. & Tielens, A. G. G. M. 1997, Ann. Review of Astronomy and Astrophysics, 35, 179

Hunter, S.D. et al. 1997, ApJ, 481, 205

Kramer, C., Alves, J., Lada, C. J., Lada, E. A., Sievers, A., Ungerechts, H., & Walmsley, C. M. 1999, AA, 342, 257

Lada, C. J., Lada, E. A., Clemens, D. P., & Bally, J. 1994, ApJ, 429, 694

Le Petit, F., Nehme, C., Le Bourlot, J., & Roueff, E. ApJS, 164, 506

Leroy, A.K., Walter, F., Bigiel, F., Usero, A., Weiss, A., Brinks, E., de Blok, W.J.G., Kennicutt, R.C., Schuster, K-F., Kramer, C., Wiesemeyer, H.W., Roussel, H. 2009, AJ, 137, 4670

Liszt, H. S. 2007, AA, 476, 291

Lombardi, M. & Alves, J. 2001, AA, 377, 1023

Lombardi, M., Alves, J., Lada, C. J. 2006, AA, 454, 781

Lombardi, M., Alves, J., Lada, C. J. 2011, AA, 535, 16

Megeath, S. T., Gutermuth, R., Muzerolle, J., et al. 2012, AJ, 144, 192

McKee, C. F. & Ostriker, E. C. 2007, Annual Review of Astronomy and Astrophysics, 45, 565

Mouschovias, T. C., Spitzer, Jr., L. 1976, ApJ, 210, 326

Narayanan, D., Krumholz, M.R., Ostriker, E.C., & Hernquist, L. 2012, MNRAS, 421, 3127

Omont, A. 2007, Reports on Progress in Physics, 70, 7, p. 1099, Fukui, Y., & J.-P. Bernard 2012, AA, 543, 103

Paradis, D., Dobashi, K., Shimokura, T., Kawamura, A., Onishi, T., Fukui, Y., Bernard, J.-P. 2012, AA, 543, 103

Pilliteri, I., Wolk, S.J., Megeath, S. T, et al. 2012, submitted to ApJ

Pineda, J.E., Caselli, P., & Goodman, A.A. 2008, ApJ, 679, 481

Pineda, J. L., Goldsmith, P. F., Chapman, N., Snell, R. L., Li, D., Cambresy, L., Brunt, C. 2010, ApJ, 721, 686

Rachford, B.L. et al. 2009, ApJS, 180, 125

Rieke, G.H. & Lobofsky, M.J. 1985, ApJ, 288, 618

Skrutskie, M. F., R.M. Cutri, R. Stiening, M. D. Weinberg, S. Schneider, J. M. Carpenter, C. Beichman, R. Capps, T.

Chester, J. Elias, J. Huchra, J. Liebert, C. Lonsdale, D. G. Monet, S. Price, P. Seitzer, T. Jarrett, J. D. Kirkpatrick, J. Gizis, E. Howard, T. Evans, J. Fowler, L. Fullmer, R. Hurt, R. Light, E. L. Kopan, K. A. Marsh, H. L. McCallon, R. Tam, S. Van Dyk, and S. Wheelock, 2006, AJ, 131, 1163.

Strong, A. W., Bignami, G. F., Bloemen, J. B. G. M., Buccheri, R., Caraveo, P. A., Hermsen, W., Kanbach, G., Lebrun, F., Mayer-Hasselwander, H. A., Paul, J. A., & Wills, R. D. 1982, AA, 115, 404

Strong, A. W. & Mattox, J. R. 1996, AA, 308, L21

Tafalla, M., Maardones, D., Myers, P.C., Caselli, P., Bachiller, R., Benson, P.J. 2002, ApJ, 504, 900

van Dishoeck, E. F. & Black, J. H. 1988, ApJ, 334, 771

Visser, R., van Dishoeck, E. F., & Black, J. H. 2009, AA, 503, 323

Whittet, D. C. B. 2003, Dust in the galactic environment (Institute of Physics Publishing Bristol, 2nd edn.)

Williams, D. A. 1985, QRAS, 26, 463

Williams, D. A., Hartquist, T. W., & Whittet, D. C. B. 1992, MNRAS, 258, 599

Wolfire, M.G., Hollenbach, D. & McKee, C.F. 2010, ApJ, 716, 1191

Young, J.S. et al. 1995, ApJS, 98, 219